Experimental investigation of the performance of a diffuser-augmented vertical axis wind turbine

by

Arash Akhgari

B.Sc, University of Tehran, 2007

A Dissertation Submitted in Partial Fulfillment

of the Requirements for the Degree of

MASTER OF APPLIED SCIENCES

in the Department of Mechanical Engineering

University of Victoria

Supervisory Committee

Experimental investigation of the performance of a diffuser-augmented vertical axis wind turbine

by

Arash Akhgari

B.Sc, University of Tehran, 2007

Supervisory Committee

Dr. Peter Oshkai, (Department of Mechanical Engineering)

Supervisor

Dr. Curran A. Crawford, (Department of Mechanical Engineering)

Departmental Member

Dr. Brad Buckham, (Department of Mechanical Engineering)

Departmental Member

Abstract

Supervisory Committee

Dr. Peter Oshkai, (Department of Mechanical Engineering)

Supervisor

Dr. Curran A. Crawford, (Department of Mechanical Engineering)

Departmental Member

Dr. Brad Buckham, (Department of Mechanical Engineering)

Departmental Member

The performance of a vertical axis wind turbine with and without a diffuser was studied using direct force measurement technique applied to a scaled model of the rotor in a water tunnel. The experiment was conducted at different tip-speed ratios. The maximum power coefficient for the turbine was found to be equal to 0.35 for the rotor with diffuser and to 0.26 for the rotor without diffuser. Therefore, the maximum power coefficient was increased by 35% when the diffuser was used in the configuration.

In the second part of this work, the flow patterns downstream of the turbine were studied by the particle image velocimetry (PIV) technique. Six different tip-speed ratios were considered for each configuration (with and without a diffuser). The vorticity and the streamline plots provide insight into the flow physics in each configuration. In addition, the swept area of a full-scale rotor was calculated for both a diffuser-augmented and a bare turbine for a range of power outputs.

Table of Contents

List of Tables

List of Figures

Acknowledgments

I would like to express my sincere gratitude to my supervisor, Dr. Peter Oshkai for his encouragement, guidance, and support during my study and research from the initial to the final step. I attribute the level of my Masters degree to his encouragement and effort and without him this thesis would not have been completed or written.

I am indebted to ARIA Wind Power Systems Inc. and its President, Christopher O'Brien Wheeler for all the supports and guidance.

I would like to extend my thanks to the people that were directly involved with the development of this work, senior scientific assistant Rodney Katz for all of his supports and patience, Peggy White and Sue Walton from the IESVic office and Dorothy Burrows and Erin Robinson for their help.

Finally I owe my loving thanks to my parents and my brother Ehsan, and my friends, Setareh, Ramtin, Naser, Muhammad, Peyman, Arash, Oleksandr, Pato, Cata, Shane and many others. Without their encouragement, understanding, and loving support it would have been impossible for me to finish this work.

Dedication

To my mother and father

CHAPTER 1

Introduction

1.1 Background

Wind turbines, which have been used for more than 3000 years, convert the kinetic energy of wind into mechanical energy. Although for many years the main application of wind turbines was limited to windmills, due to the oil crisis in 1973 and the sudden increase in the price of oil, the wind turbine technology was supported by the governments of several countries as an alternative to fossil fuels for producing electricity on a large scale.

Although the wind power was used to sail for more than 5000 years, the first wind machines were used in Persia as early as 200BC. The first windmills were invented in Sistan, Iran in 7th century [1]. Those windmills were of the vertical axis type, with long vertical blades. They were used to grind corn and pump water [1]. Figure 1.1 presents a sketch of the first windmills in Persia with the image of the windmill structure [2].

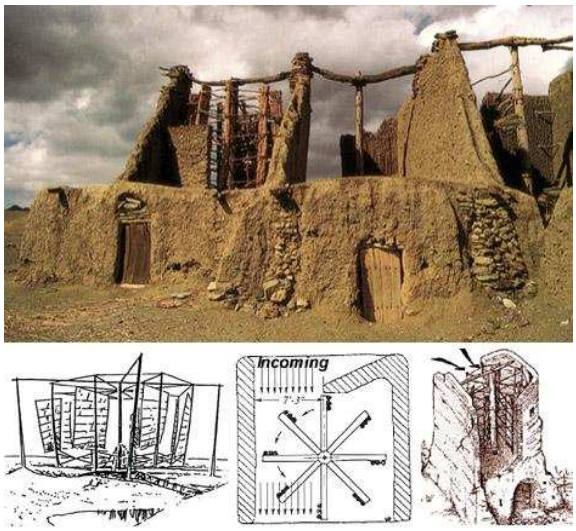

Figure 1.1 – Ancient Persian windmill [2]

The first electric wind turbine was built in Scotland in 1887 and a larger one was built in Cleveland, Ohio in 1888 by Charles Brush. Charles Brush wind turbine had a rotor with 17 m diameter and was installed on an 18m long base. His turbine has generated 12 kW of power. A picture of Charles Brush wind turbine is presented in Figure 1.2 [3].

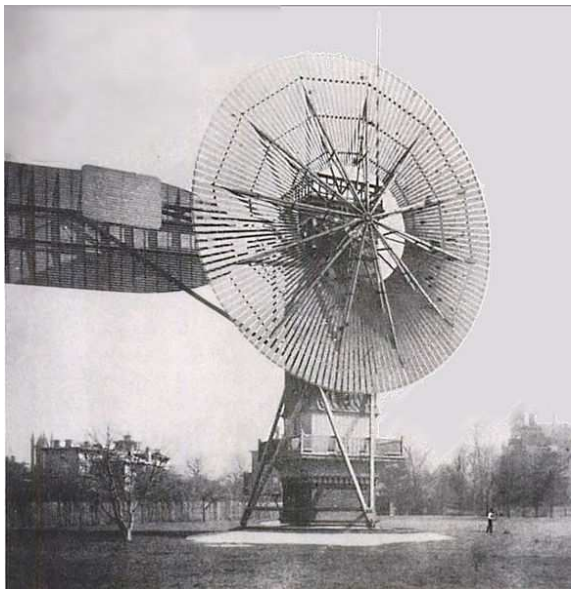

Figure 1.2 - Charles Brush wind turbine, Cleveland, Ohio

More detailed historical development of windmills and wind turbines is documented in a book by Spera, which is titled “Wind Turbine Technology” [4].

Wind turbines can be categorized into two types based on the axis in which the turbine rotates, which are horizontal axis wind turbines (HAWT) and vertical axis wind turbines (VAWT). In HAWTs, the blades of the turbine rotate around a horizontal axis and they are usually pointed into the wind direction. On the other hand, VAWTs are a type of wind turbine in which the main rotor shaft operates vertically [5]. Compared to the HAWTs, the VAWT has several advantages. Firstly, the VAWT is independent of the wind direction, hence there is no need to design a control system for the direction adjustment of the blades, and also the turbine can be used in places, where the wind direction is highly variable. Secondly, the generators and gearboxes can be placed close to the ground, which results in lower load on the tower and easier maintenance. The installation cost of the VAWT is also lower than the HAWT. Furthermore, the noise produced by the blades of certain types of VAWTs is lower due to the lack of blade tips and the ground-mounted drive train. On the other hand, the major disadvantage of the VAWT is the relatively low power output for the same swept area of the blades, compared to a HAWT [6].

Figure 1.3 shows a HAWT near Aalborg, in Denmark and three different VAWTs. Figure 1.3 (b) presents a Darrieus wind turbine Magdalen Islands in Canada. Figure 1.3 (c) shows a Giromill (also known as H- Darrieus) rotor and Figure 1.3 (d) presents a Savonius wind turbine.

(a)

(b)

(c)

(d)

Figure 1.3 – a) A horizontal axis wind turbine in Aalborg, Denmark b) A Darrieus vertical axis wind turbine (lift based) in Magdalen Islands, Canada c) A Giromill vertical axis wind turbine (lift based) d) Savonius vertical axis wind turbine (drag base) ((a) and (b) are taken from http://www.solarnavigator.net/, (c) and (d) are taken from http://www.thegreentechnologyblog.com/)

With the potential flow assumption for the air, the power output of the wind turbines can be expressed by the following equation,

$$P = {}^{1}/_{2} C_p \rho A U^3, \quad (1.1)$$

where C_p is the power coefficient, ρ is the air density, A is the swept area of blades, and U is the wind speed [5]. The power coefficient C_p , which also represents the efficiency of the turbine, is defined as the ratio of the extracted power to the available power. The theoretical upper bound of the power coefficient is 0.593 (Betz limit) for conventional free stream wind turbines [5].

Figure 1.4 illustrates a schematic for the energy extraction in a HAWT by showing a stream tube of the wind flow. It is assumed that the air has not been compressed while passing through the rotor. The cross section of the stream tube must expand to maintain constant flow rate [5].

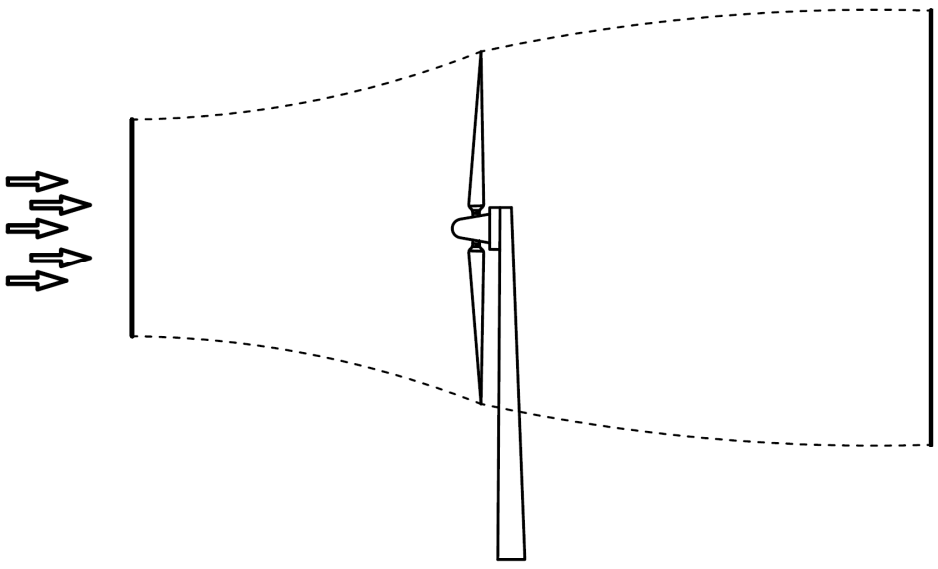

Figure 1.4 – Stream tube of the wind passing through turbine

The air static pressure downstream of the rotor is less than the surrounding air pressure level. Also, the air velocity is decreased in the downstream. The region downstream of the rotor is called the wake region. The static pressure must be increased at the far wake to match the atmospheric condition. Therefore, there is no change in the static pressure across the rotor from far upstream to far downstream, but the kinetic energy of the flow is reduced [5].

1.2 Diffuser-Augmented Wind Turbine

One of the main goals of wind turbine development is increasing the power output of the turbine. According to the equation (1.1), there are two parameters that affect the value of the power - the swept area of blades and the wind speed. Therefore the power output can be increased by increasing one of those two parameters. According to the Betz limit, for the conventional wind turbines the power coefficient is a limited parameter. One of the methods to increase the effective wind velocity is to use a duct around the rotor. That design sometimes referred as a Diffuser-Augmented Wind Turbine (DAWT). Figure 1.5 illustrates a schematic of this design applied to a HAWT and the change in the stream tube comparing to the conventional (free-stream) wind turbine.

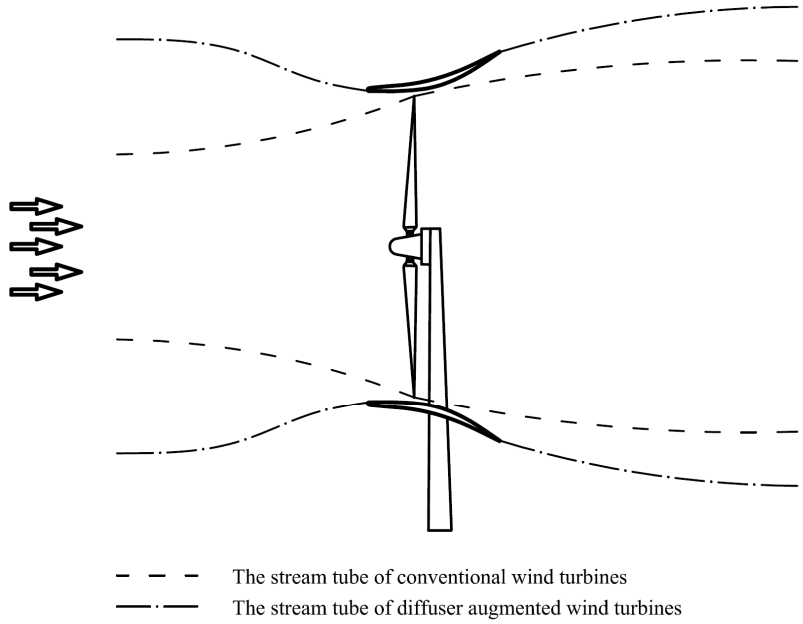

Figure 1.5 – Stream tube comparison between a conventional wind turbine and a DAWT

The duct around the rotor increases the flow rate of the air trough the area swept by the rotor, thus increasing the wind velocity at the rotor. Therefore the effective range of the wind speed for generating the desired power is wider than that corresponding to the conventional design. DAWTs also have higher power per unit of rotor area than the turbines without diffuser. Another advantage of using a diffuser around the blades is that the theoretical maximum power of ducted wind turbine is not limited by the Betz limit, and is related to the pressure difference and the flow rate in the duct [7]. By analytical simulation, Riegler [8] demonstrated that the maximum power coefficient of the diffuser shape ducted wind turbine is 3.3 times higher than the Betz limit for a free-stream turbine.

One of the disadvantages of using the diffuser is that the overall weight of the structure is increased and using the diffuser makes the design more complicated. Also,

putting a diffuser around a VAWT eliminates the independence of the turbine on the wind direction, which is one of the most important advantages of VAWTs.

Several studies regarding the diffuser design for the HAWTs have been reported in literature. One of the early investigations for the diffuser-augmented wind turbines was done by Igra [9]. In that experimental study the author used a NACA 4412 airfoil as a diffuser around a HAWT to present the power improvement by a factor of two. In his later work [10], Igra investigated different NACA airfoils for the diffuser-profile and also different designs by using a airfoil-ring behind the diffuser and also an airfoil-ring at the entrance.

One of the most recent diffuser designs was done by Abe et al. [11]. The authors suggested a diffuser with a flange at the end of the diffuser to increase the power output of a HAWT. In that work, the authors performed a numerical and experimental investigation to show the effect of the flange downstream. They also investigated the effect of the entrance of the diffuser by using a diffuser with wider entrance section. The flanged diffuser was used for a further experimental study of Ohya et al. [12] to design a commercial diffuser-augmented turbine. Furthermore, Ohya at al. studied the flange at the end of the diffuser for different diffuser length to design more compact diffusers [13].

Although the majority of the diffuser developments were done for HAWTs, there are few works that focused on diffuser design for VAWT applications. In particular, Takahashi et al. [14], studied performance of a Darrieus vertical axis wind turbine with a flanged diffuser. The authors compared the performance of the bare rotor with two

different flanged diffusers. Furthermore, a numerical and experimental investigation were done by Roa et al. for a cross flow water turbine with and without diffuser [15]. The authors used a darrieus-shaped rotor for tidal application with two different airfoil profiles for the diffuser.

1.3 Experimental studies of Horizontal and Vertical axis wind turbines

Since the horizontal axis wind turbines are largely used to generate the power, there are several numerical and experimental studies related to the HAWTs application. Whale et al [16] studied the wake structure of a wind turbine experimentally in a water tunnel, using a small-scale turbine. The authors compared the experimental results with a numerical calculation based on Rotor Vortex Lattice Method and a custom code. The authors also validated the experiment by a full-scale experiment in a wind tunnel [17]. Moreover, Grant [18] studied the trailing vortex shading form the blades of a HAVT in yaw by the particle image velocimetry (PIV) method in the wind tunnel. Furthermore, Toshimitsu et al. studied the flow structure of a wind turbine with the flanged-diffuser [19]. The authors used the PIV technique to illustrate the flow pattern behind the diffuser and in the cross section of the rotor. The authors used the diffuser design which was introduced by Ohya et al. [12, 13]. In their study, the authors introduced the formation of blockage vortices behind the diffuser due to the pressure drop.

Even though Savonius vertical axis wind turbines are not widely used due to the low power output of the turbine, there are some experimental studies of this type of

turbines. Fujisawa [20] studied a two-bladed Savonius rotor inside a water tunnel to illustrate the flow pattern inside and around the rotor by using the PIV method. Then the authors compared the experimental results with the numerical calculation to validate their numerical simulation.

Two of the more recent experiments regarding Savonius VAWTs were performed by Saha et al. [21] and Murai et al. [22]. Saha et al. investigated the effect of twisted blade on a three-bladed Savonius rotor to study the feasibility of further development of the turbine. The authors measured the power output of the turbine with different twisting angles with comparison to the untwisted blade rotor inside a wind tunnel [21]. Murai et al. illustrated the pressure field around a two-bladed Savonius rotor by performing an experiment inside a water tunnel. The authors discussed the influence of the lift force during one rotation of the rotor along side with the drag force [22].

Most of the experiments on the Darrieus VAWTs were done to investigate the dynamic stall of the blades in one rotation of the rotor, since operation of Darrieus wind turbine directly causes the dynamic stall of the blades. Ferreira et al. [23] studied the dynamic stall of a straight-blade Darrieus-rotor by an experiment which was conducted in a wind tunnel. In that experiment, the authors visualized the dynamic behaviour of one blade of a Darrieus-rotor in one rotation by using the Particle Image Velocimetry (PIV) method. Afterward, the authors used the PIV images to validate a 2D numerical study which was used for further development of the VAWT application [24].

By an experiment which was carried out by Shaibuya and Fujisawa [25], the vortex structure of a one-bladed rotor was studied by using the PIV technique. They used a

rotating frame of reference for the experiment, and they used a small scale rotor inside the water tunnel to perform the PIV. Furthermore they extended their study from the rotating frame of reference to a stationary frames of reference [26].

Although most of the studies on the VAWTs were focused on the flow structure inside the rotor, Roa et al. [15] studied the wake region behind a Darrieus-shaped rotor water turbine. In their study, Roa et al. focused on developing a diffuser for the presented turbine. The authors studied the flow pattern inside the rotor and behind the rotor and diffuser to compare the rotor performance with and without diffuser.

1.4 Particle Image velocimetry (PIV) Fundamentals

To study the wake structure of the flow in the current study, particle image velocimetry (PIV) method was used. PIV is an optical method that is used to visualize the flow and to calculate the velocity field which can be used for further study of the flow. This method was used for many different applications such as the velocity field calculation in thermal convection, boundary layer studies, transonic flows of a jet or around an airfoil, vortex shading of a body inside a flow and wind and water tunnel experiments [27].

PIV is a method for measuring the fluid velocity in a two-dimensional cross-section of the flow field. This evaluation of velocity is done by recording the location of the images of the seeding particles in the fluid at two or more time intervals. Subsequently, by calculating the displacement of each particle (Δx and Δy) and by knowing the time interval between the images (Δt), the velocity of each particle can be calculated.

According to the fundamental definition of velocity, the velocity components of each particle equal to $u(x,t)= [\Delta x (x, t)]/\Delta t$ and $v(y,t)= [\Delta y (y, t)]/\Delta t$ where u is the velocity component in the x-direction and v is the velocity component in the y-direction. To measure the displacement, each observation is divided to several sections (interrogation windows). Then, the displacement of the particles inside the specific interrogation window is calculated. Assuming constant velocity for all the particles inside a single interrogation window, a single velocity vector can be calculated representing the particles in the interrogation window.

A general review of Particle Imaging Techniques is given by Adrian [28]. The author gives a brief description of the various particle imaging techniques such as Pulsed-Light Velocimetry and Particle-Image Velocimetry. The author mentioned three modes of operation for PIV, laser-speckle mode (LSV), particle-tracking mode (PTV) and high image-density mode.

Adrian categorized PIV in six different groups, which are different types of Pulse Codes which consist of different number of frames and pulses. They are Single frame/Single pulse, Single frame/Double pulse, Single frame/Multiple pulse, Multi-frame/Single pulse, Multi-frame/Double pulse, Multi-frame/ Multiple pulse. According to different illumination pulse from the laser, there are different image patterns in each of the methods. Concerning single-frame recording, the final image can be recorded on a one frame of film or on an electronic frame of video camera. On the other hand *Multiframing* usually applies to cinematic film or sequences of video image frames [28].

There are four general methods for calculating the velocity form the images which are recorded: Direct Autocorrelation (also known as Autocorrelation), Direct Cross Correlation (also known as Cross Correlation), Young's Fringes, and Optical Correlation [29].

In the autocorrelation method, the whole picture of the particle images can be digitized and fed into a computer and the velocities can then be obtained by autocorrelation. In such techniques particle images are usually taken on a film which enables high resolution measurements [30]. Large velocities can thus be measured where the time interval between two exposures may be very small.

In the cross-correlation method, spatial cross-correlations between two sequentially exposed flow pictures are used to determine the velocities [31]. This technique removes the so called directional ambiguity which is inherent in the other techniques.

In Young's fringe method the sequentially double- or multi-exposed particles are first recorded in a single flow picture. Since these particle images are self-correlated, Young's fringes can be used to extract the velocities [32]. Young's Fringes method uses a lens, which perform a two dimensional Fourier transform of the light wave from the interrogation window. Then the intensity of the Fourier transform is measured a distance L from the lens.

The optical correlation is a two-dimensional correlation function of an interrogation window that can be formed optically by replacing the two digital FFT operations with optical Fourier transformations [29].

At present, the cross correlation method is the most popular technique to calculate the velocity field for the PIV method. In this technique, two sequential digital images are divided into interrogation windows. Using these images, the spatial shift of the seeding particles is generated. Two sample regions *f(m, n)* and *g(m, n*), spatial function *s(m, n)* and a noise process *d(m, n)* are considered where *m* and *n* are the coordinates of the interrogation window. The sample region *g(m, n*) is the result of translation of *f(m, n)* using the spatial function. This region can be calculated by using the following equation (spatial convolution of *f(m, n)* and *s(m, n)*) [33]:

$$g\,(m,\,n) = \left[\sum_{k=-\infty}^{\infty} \sum_{l=-\infty}^{\infty} s(k-m, l-n)\; f\,(k,l) \right] + d\,(m,n)\,, \tag{1.2}$$

The displacement function can be found using the discrete cross-correlation function $\phi_{fg}(m,\,n)$ of the sampled regions [33].

$$\phi_{f\,g}\,(m,\,n) = \frac{\sum_{k=-\infty}^{\infty} \sum_{l=-\infty}^{\infty} f\,(k\,,l)\; g(k+m, l+n)}{\sum_{k=-\infty}^{\infty} \sum_{l=-\infty}^{\infty} f\,(k\,,l) \sum_{k=-\infty}^{\infty} \sum_{l=-\infty}^{\infty} g(k\,,l)}\,, \tag{1.3}$$

If the value of $\phi_{fg}(m,\,n)$ approaches unity, it means that many particle images match up with their corresponding spatially shifted partners. The highest correlation peak is considered to represent the best match of particle images between the two sampled functions [33].

Figure 1.6 shows a flowchart of the cross-correlation PIV procedure. In this process, the complex conjugate multiplication is used to estimate the cross-correlation

in the frequency domain by using fast Fourier transforms (FFT) to simplify and to increase the speed of the process. The cross correlation technique removes the directional ambiguity, which is inherent in both the Young's fringe and autocorrelation techniques [33].

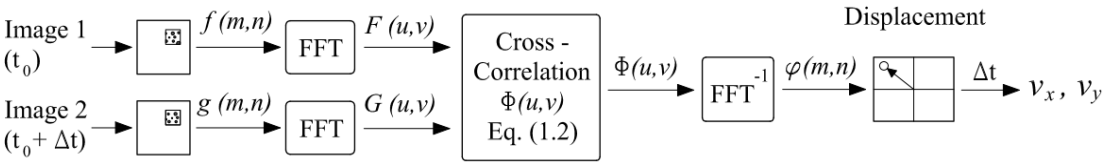

Figure 1.6 - Numerical processing flow-chart of PIV method [33]

The velocity, which is calculated at the end of the numerical procedure, is considered as the interrogation window's velocity. Therefore, the velocity of all particles in the window is assumed to be the same. To reduce the error caused by this assumption and also to increase the resolution of the velocity field, an overlapping amount is chosen between the windows. For example if a 75% overlapping is chosen, there are 9 generated velocity vectors in each interrogation window.

One method to refine the velocity value for each window is to divide each window to 9 cells (3 by 3 divisions) and replace the center data vector of each window with the average of the 3 by 3 data. Therefore the result is to eliminate the high frequency jitter caused by the different location estimates of the peak correlation [33].

The sources of error in the calculation of velocity field can be categorized as follows [30], [33]:

(a) Noise, which is a random function of time and space.

(b) System error, which is a function of the location.

(c) Turbulent flow motions.

(d) Out-of-pattern motions, which occur when either particles imaged in the interrogation window move out of the area in the next image in process, or when particles which are not imaged in the interrogation window move into that in the next image in process.

(e) Flow velocity gradients, which are $\partial u/\partial x$, $\partial u/\partial y$, $\partial v/\partial x$ and $\partial v/\partial y$ in the 2-d flow which causes different velocity for the particles in one interrogation window.

The PIV setup which was used in the current experiment as well as the error analysis is discussed in Section 2.5.

1.5 Objectives

The primary goal of the current research is to improve the power output of a vertical axis wind turbine. It is proposed to achieve this goal by adding a diffuser around the rotor. Several experiments were performed to measure the power output of the turbine using a direct torque measurement technique. The experiments were conducted in a water channel with a small-scale turbine model. The experiments focused on calculating the efficiency of the turbine *without* and *with* a diffuser to investigate the influence of the diffuser on the turbine performance.

The secondary objective of this research is to study the flow patterns downstream of the turbine. The flow visualization was performed using the PIV technique. The flow

patterns were used to study the dynamic flow behaviour behind the rotor and diffuser and to visualize the effects of the diffuser on the formation of the wake region behind the rotor. Furthermore, the flow visualization can be used to validate the numerical simulation which can be used for further development of the diffuser.

Finally, the system size of the turbine *with* and *without* diffuser, corresponding to a desired power output, was calculated.

1.6 Thesis overview

Chapter 2 of the thesis contains an overview of the experimental apparatus and the devices that were used to determine the power output of the system in conjunction with the flow visualization. The design procedure of the experimental apparatus is also discussed in detail. The challenges of the small-scale model implementation were overcome during the design of the experimental apparatus, which is also discussed in Chapter 2. Also, the motion control and the direct torque measurement techniques are introduced, and the PIV setup of the current experiment is discussed.

Chapter 3 presents the results of the investigation, along with the corresponding discussion. The power output and performance curves of the turbine *without* and *with* diffuser are presented in Chapter 3, along with the flow visualization results.

Afterward, the power output and the performance of two designs are compared to discuss the influence of the diffuser in detail. The flow structure behind the diffuser is also used for further discussion on the power output difference between the designs.

Finally the system size of the turbine is discussed in the last part of Chapter 3 to present the actual size of the turbine *without* and *with* diffuser, corresponding to the identical power output.

In the end, the conclusions and the recommendations for future are presented in Chapter 4.

CHAPTER 2

Experimental system and techniques

2.1 Flow Facility

The experimental study of the performance of a diffuser-augmented wind turbine was done in the flow visualization water tunnel in the Fluid Mechanics Laboratory of the Department of Mechanical Engineering at the University of Victoria.

A water tunnel is an experimental facility which is used to study the hydrodynamic behaviour of submerged bodies in flowing water. The water tunnel is similar to a re-circulating wind tunnel, except that the working fluid is water, instead of air. With proper scaling, the experiments can be conducted with a small-scale turbine model. The other difference between water and air tunnels is the way that the driving force is generated in each system. The driving force in an air tunnel is usually provided by a multi-blade impeller. On the other hand, in a water tunnel, the fluid is circulated by a pump.

The water tunnel which was used for the current study was a closed loop re-circulating type. This tunnel consisted of a test section, a filtering station and a circulating pump with a variable speed drive assembly. The test section was 2.5 meters long and has a 45 cm^2 cross section. The water tunnel is shown in Figure 2.1.

Figure 2.1 – Water tunnel which was used in the experiment

2.2 Experimental apparatus

The objective of the current experimental study is to investigate the effect of a diffuser around the rotor of a VAWT. Two effects of the diffuser were studied in this experiment. The first effect was the change of power output of the turbine, and the second one was the change of flow characteristics behind the rotor.

A 2D cross section (front view) of the experimental apparatus is shown in Figure 2.2. The major parts of the apparatus are indicated by different colors, and each color was labelled in the legend of the schematic. A 3D schematic and a picture of the experimental apparatus are presented in Figures 2.3 and 2.4, respectively.

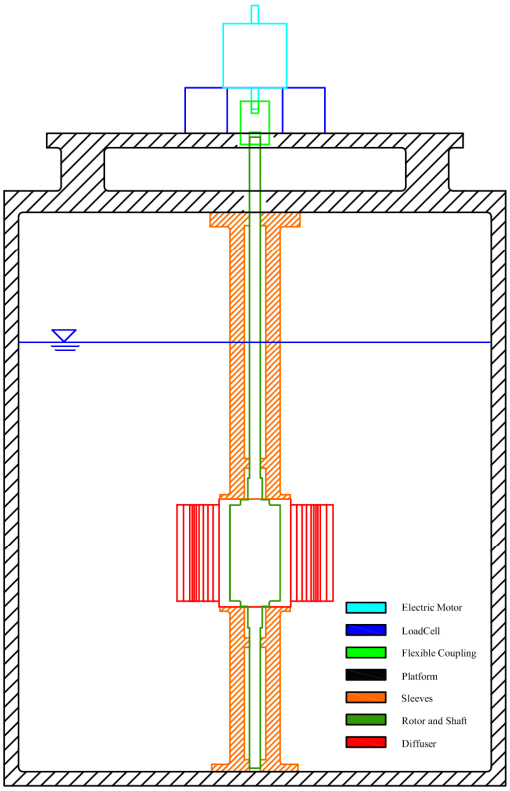

Figure 2.2 – Cross-section schematic of the experimental apparatus

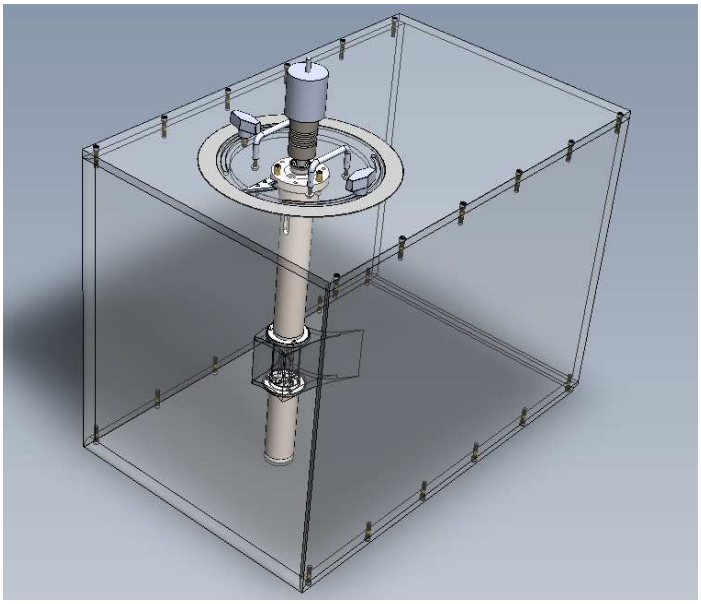

Figure 2.3 – Isometric view of the experimental apparatus

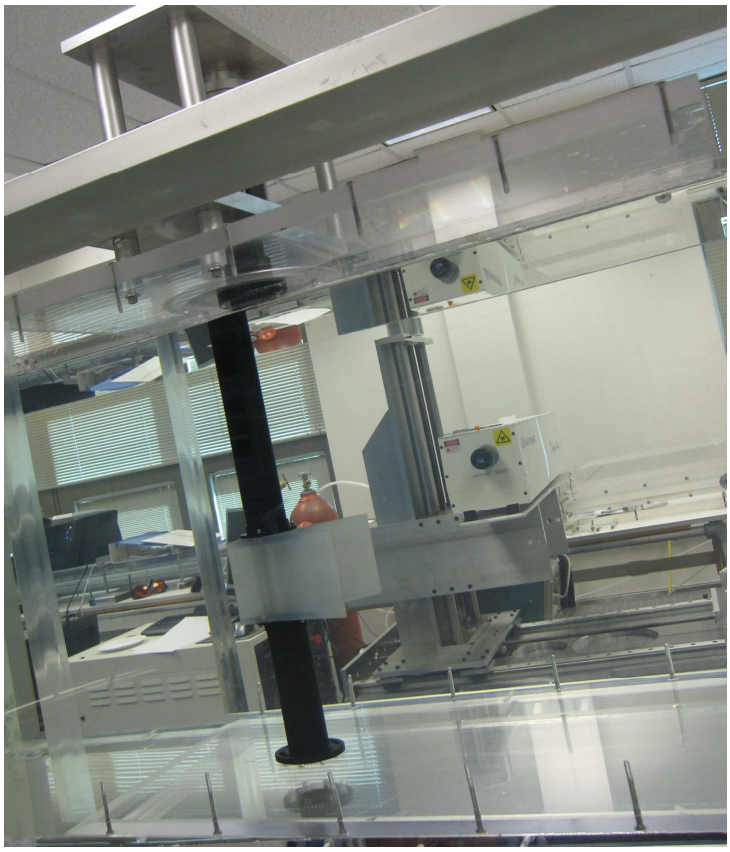

Figure 2.4 – Experimental setup inside the water tunnel

In order to scale the model, the kinematic similarity was chosen to match the tip-speed ratios of the model inside the water tunnel and the actual full scale model in the air. The tip-speed ratio (λ) is a dimensionless number which can be defined by the following equation

$$\lambda = R\omega/U, \tag{2.1}$$

where R is the rotor radius (m), ω is the rotating speed (rad/sec) and U is the flow velocity (m/s). Therefore this ratio is the ratio of the tip-speed of each blade and the inflow velocity.

The tip-speed ratio is analogous to the Strouhal number ($St=\omega L/U$, where L is the characteristic length) for the turbine applications. For an experiment conducted in the water tunnel, the Reynolds number ($Re=CU/\upsilon$, where C is the chord length of the blades and υ is the fluid viscosity) is two orders of magnitude lower than the Re of the full-scale turbine [34].

For the geometric similarity between the model and the full scale turbine, a scaling factor of 0.059 was selected. The scaling parameters of the model used in the water tunnel, as well as those of the full-scale turbine are summarized in Table 2.1.

Table 2.1 - Scaling parameters of the turbine model

Parameter	**Air**	**Water**
Density (kg/m^3)	1.205	998.29
Kinematic Viscosity (m^2/s)	1.511 E -05	1.0047 E -06
Temperature (°C)	20	20
Velocity, **U** (m/s)	10	0.5
Blade Chord, C (mm)	254	15
Rotor Radius, R (mm)	381	22.5
Reynolds Number, Re (Based on Chord length)	1.91 E +05	8.517 E +03
Diffuser dimensions:		
Entry Section (mm)	1040	61.4
Exit Section (mm)	2320	137
Length (mm)	2230	131.7

The cross-section drawing of the rotor and the diffuser of the model is shown in Figure 2.5, with dimensions being in mm. The rotor geometry used in the current study

corresponded to the rotor used in an earlier numerical investigation by Bouhadji and Oshkai [35]. The rotor was an optimized design of a vertical axis wind turbine produced by PacWind Inc. The rotor is a cross-flow type, lift and drag base, with six blades. Each blade had a pitch angle of 60 degree.

The diffuser profile which was used in the current study was based on a geometry which was suggested by Riegler [8]. Riegler showed that by using this profile for the diffuser around a vertical axis wind turbine, the power coefficient is no longer limited by 0.59 [8]. In Figure 2.5, the flow passes from right to left of the picture. The entrance of the diffuser, which is at the left hand side of the picture, has a horizontal profile. The exit section, which is at the right hand side, has an angle of 35 degree by the horizontal line.

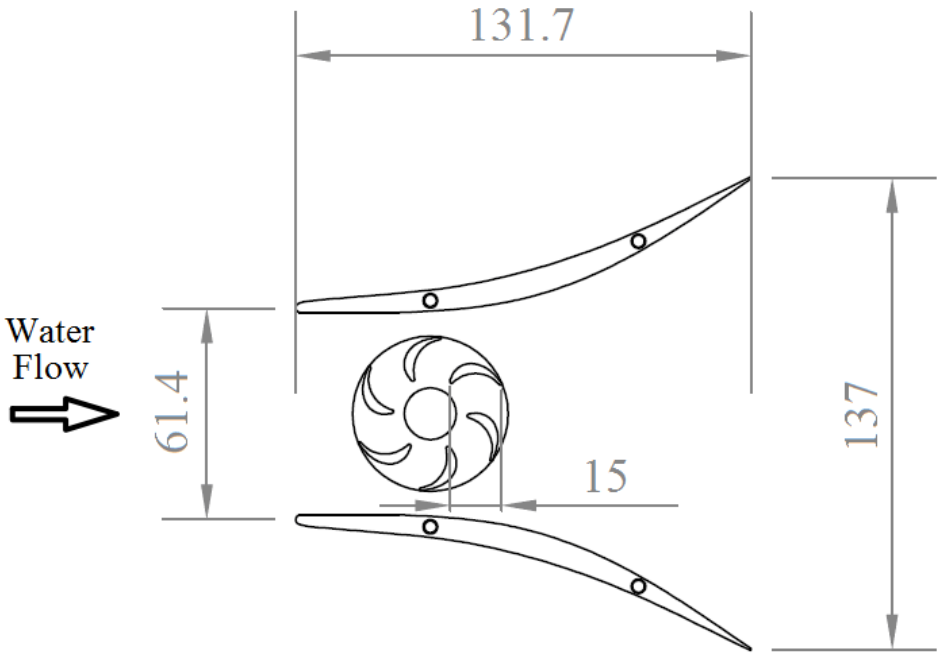

Figure 2.5 – Cross section drawing of the diffuser and the rotor (dimensions are in mm)

The rotor and the diffuser were made by the rapid prototyping Stereolithography (SLA) technique, and the material used was WaterShed XC. Figures 2.6 and 2.7 present the images of the rotor and the diffuser.

The SLA technique is one of the first rapid prototyping techniques used since the early 1980's. In this method, a powerful beam of ultraviolet (UV) light is moved by the machine’s optical scanning system across a container of photosensitive liquid polymer. The part is made of thin layers formed on top of each other. Each layer is solidified by the ultraviolet beam at the contact point of the light beam and the indicated layer. Finally the solid seamless part is generated by creating each layer separately on top of each other. The SLA was then finished by sanding.

Figure 2.6 – The rotor model made by SLA technique

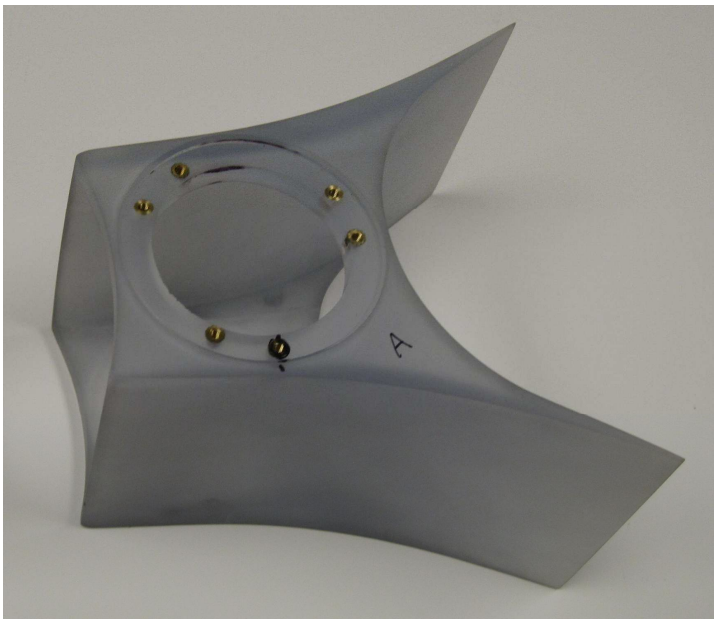

Figure 2.7 – The diffuser model made by SLA technique

The components of the experimental apparatus were assembled inside a box made of Plexiglas. The Plexiglas material provided optical access for flow visualization. The box was made with an open section at entrance and exit in order to pass the water through. Two walls at the sides and two plates at the top and bottom of the box made the alignment of the rotor with the rotating shaft all along the plates easier. The entire box containing the experimental system was placed inside the water tunnel.

In order to avoid the vibration of the system due to the rotation of the rotor, the rotor and diffuser were fixed at both sides. Two sleeves at both sides of the rotor fixed the rotating shaft with four bearings (two at each side). Each of the sleeves was attached to the top and the bottom plates of the box. The diameter of these sleeves was chosen to be the same as the rotor diameter to prevent the unwanted flow disturbance.

The sleeves were made of Delrin material, which is a trade name for polyoxymethylene plastic. One of the most important advantages of Delrin is the low friction of the material, especially when the water is used as the cooling fluid. Because of this advantage, Delrin also was used in the bearing application. Therefore, the bearings for holding the rotating shaft were made by a cut through the sleeves themselves in order to reduce the additional mechanical part in the system. Furthermore, by making the bearings in this way, water is the cooling fluid for the bearings since they are inside the water. Another function of the sleeves was to provide a technique to hold the diffuser around the rotor, since all the connecting parts to the rotor was rotating. A detailed drawing of the cut inside the sleeves is shown in Figure 2.8.

The 3D schematics of the sleeves design are depicted in Figure 2.9, (a) and (b). Figure 2.9 (a) presents the method in which the sleeves have held the rotating shaft and Figure 2.9 (b) presents the technique in which that the diffuser was fixed by the sleeves.

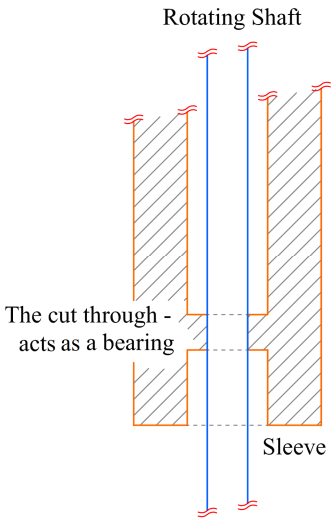

Figure 2.8 – The cut through the sleeve which acts as a bearing to hold the rotating shaft

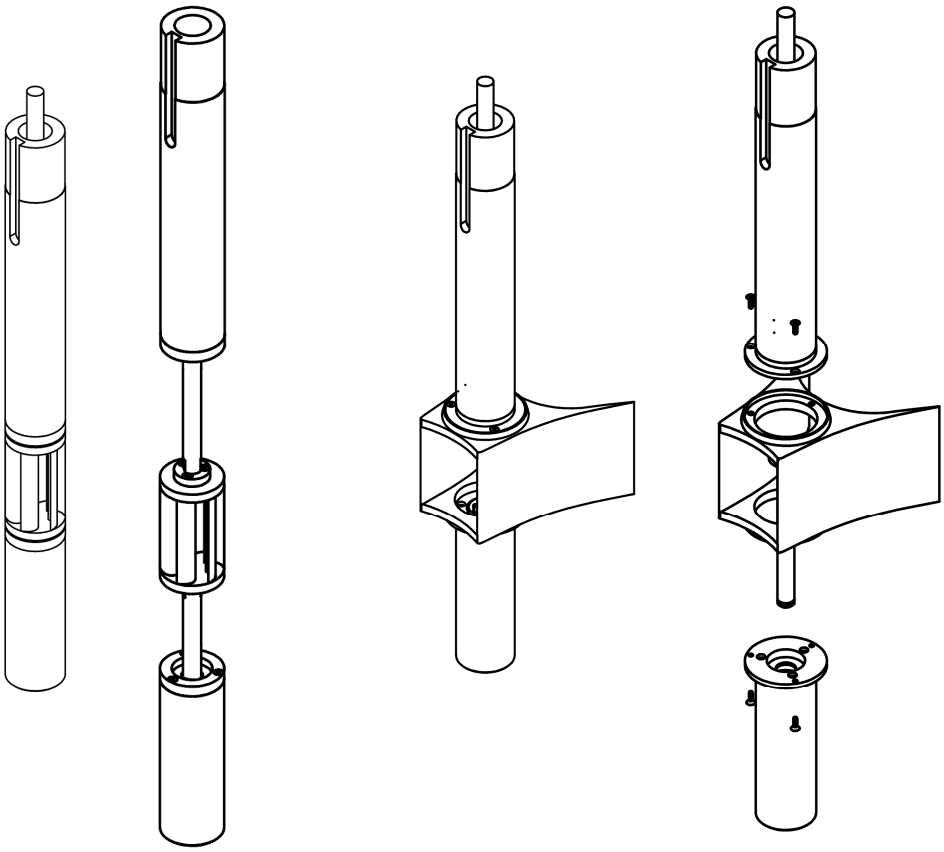

a) b)

Figure 2.9 – The 3D schematic of the sleeves with a) rotating shaft, b) diffuser

Since the performance of a VAWT with diffuser is no longer independent of the wind direction, the functionality of the diffuser as a function of the wind direction should be studied to find the applicable range of the direction change for the wind. Therefore, in the experimental apparatus, there should be a system to provide the rotation of the diffuser around the rotor to provide different angles of attack at the tip of the diffuser. The rotating system was controlled by a disk at the top of the box which was attached to the upper sleeve. Therefore the sleeves can be rotated by that disk. While the sleeves are attached to the diffuser, the diffuser rotates at the same angle as the sleeves and the

disk. Two knobs have fixed the disk to the box; therefore the diffuser was fixed during each experiment. A 3D schematic of the design is presented in Figure 2.10. An angle indicator on the disk traced the changes of the angle of attack corresponding to the diffuser.

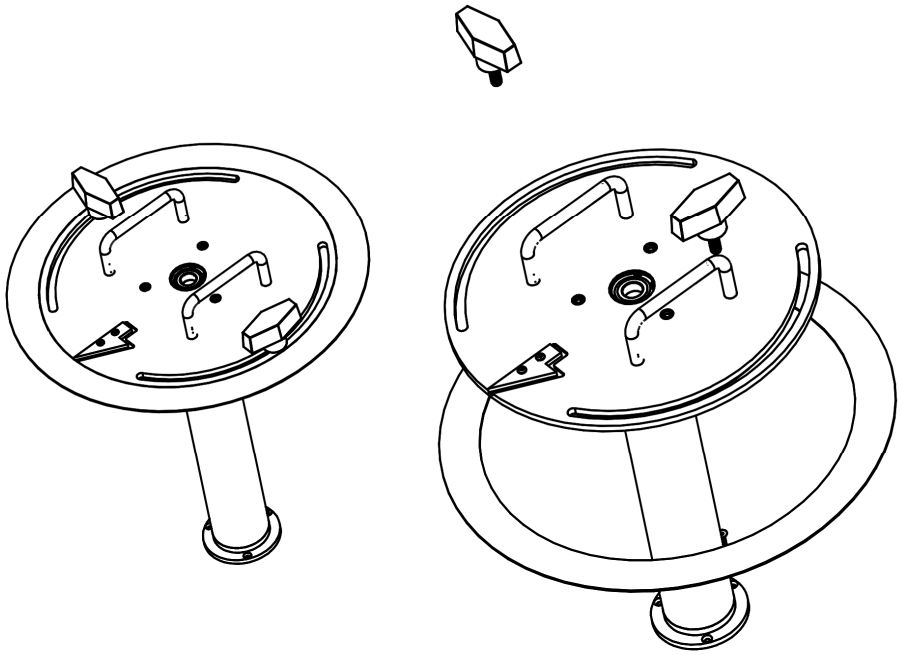

Figure 2.10 – 3D schematic of the disk that was providing the rotation of the diffuser

2.3 Motion control

The one-axis rotation of the rotor was generated by a stepper motor, HV232, manufactured by Parker Hannifin Corporation. The motor had a resolution of 25000 steps per revolution with an error of 3 – 5% per step, which is non-cumulative from one step to another. A stepper motor is a brushless, synchronous electric motor that can

divide a full rotation into a large number of steps. The motor's position can be controlled precisely without any feedback mechanism. Stepper motors are constant power devices (power = angular velocity X torque). As motor speed increases, the torque usually decreases. The main advantage of this type of motors is the variable rotating speed which eliminates the need for a gearbox.

A flexible coupling has connected the output shaft of the electric motor to the rotor shaft which has provided the vertical and angular offset for the misalignments in the apparatus. The motor was mounted on the load cell directly as long the load cell had a specific design for this experiment. The motor shaft also was passed through the load cell. The exploded view of cross section of the connections between the motor and the load cell, and between motor and the rotor shaft was illustrated in Figure 2.11.

In the present experiment, the rotating speed of the motor was set to constant. While there was no diffuser in the experiment, the rotating speed was changed form about 0.5 to 6 rps, with 0.5 rps increase after each test. In the tests including the diffuser, the rotating speed was changed from about 1 to 7 rps with 0.5 rps difference between each test. In order to calculate the power output of the turbine at different tip-speed ratios, each set of the experiments with different rotating speeds was conducted at four constant water velocities inside the water tunnel, 0.451, 0.533, 0.615 and 0.697 m/s. The range of the tip-speed ratio was varied from 0.2 to 1.6.

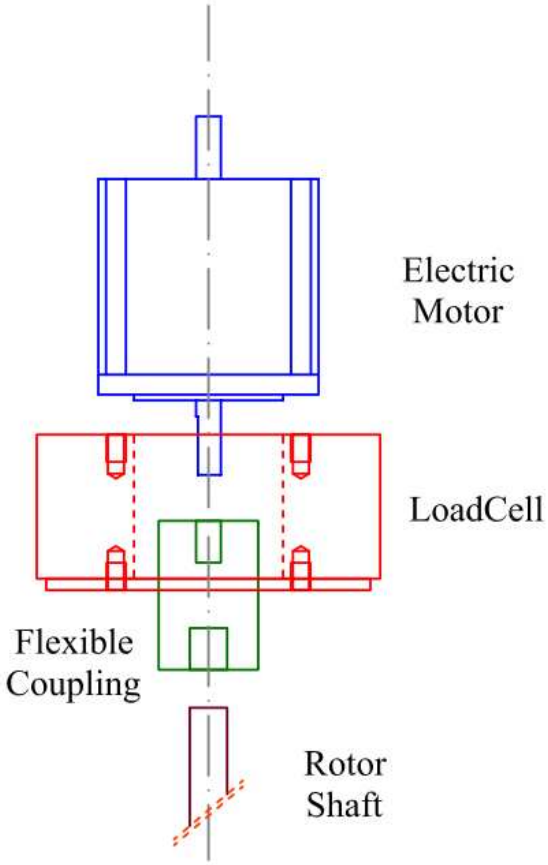

Figure 2.11 – Exploded view of the connections between the electric motor, the load cell and the rotor shaft

2.4 Direct torque measurement

The torque of the turbine was measured using a one-axis Load cell (F326-Z3878, Novatech Measurements Ltd). The load cell was connected to the LabView software through the 16-bit resolution Digital Acquisition system (DAQ). The frequency of the data acquisition was set to 1000 Hz. To average the deviation of each result, each

experiment was performed 5 times. Also for each test, the average of 20000 data points was calculated in order to get the constant and uniform torque which was imposed from the water to the rotor.

According to Figure 2.11, the motor was connected to the load cell directly; therefore there are no additional mechanical parts to reduce the mechanical loss in the torque measurement.

Figure 2.12 illustrates a filtered sample result for the rotor without diffuser at 2 rps rotating speed and 0.451 m/s water velocity. The filtering process was done by a digital filter using the MATLAB software. In order to record the data, the motor has first been started with a certain rotating speed while the water pump of the water tunnel was turned off (region (a) in Figure 2.12). After that, the water pump was turned on to a specific velocity for the test (region (b) in Figure 2.11). Finally the water pump was turned off while the motor is still running to record the residual torque of the experiment (region (c) in Figure 2.12).

Region (a) in Figure 2.12 indicates the reaction torque which was imposed to the electric motor. This reaction torque was generated as a result of the rotation of the motor. The reaction force of the water which was imposed to the blades also caused the additional reaction torque to the system.

Region (b) in Figure 2.12 indicates the torque which was imposed from the turbine to the load cell due to the water movement. This torque was generated due to the hydrodynamic force imposed by the water on the turbine due to the rotation of the blade

and due to the water flow. Therefore, the torque output of the turbine was calculated by subtracting the mean value of torque between regions (a) and (b) in Figure 2.12.

It should be noted that the hydrodynamic torque imposed by the water is, in general, different in regions (a) and (b), since the flow patterns corresponding to the rotating and the stationary rotor are different. Therefore, subtraction of the torque values corresponding to these regions does not completely eliminate the additional hydrodynamic torque imposed on the system. In the present study, this difference between the additional hydrodynamic forces corresponding to the presence and the absence of the incoming water flow was assumed to be small relative to the mechanical friction losses in the system and was neglected.

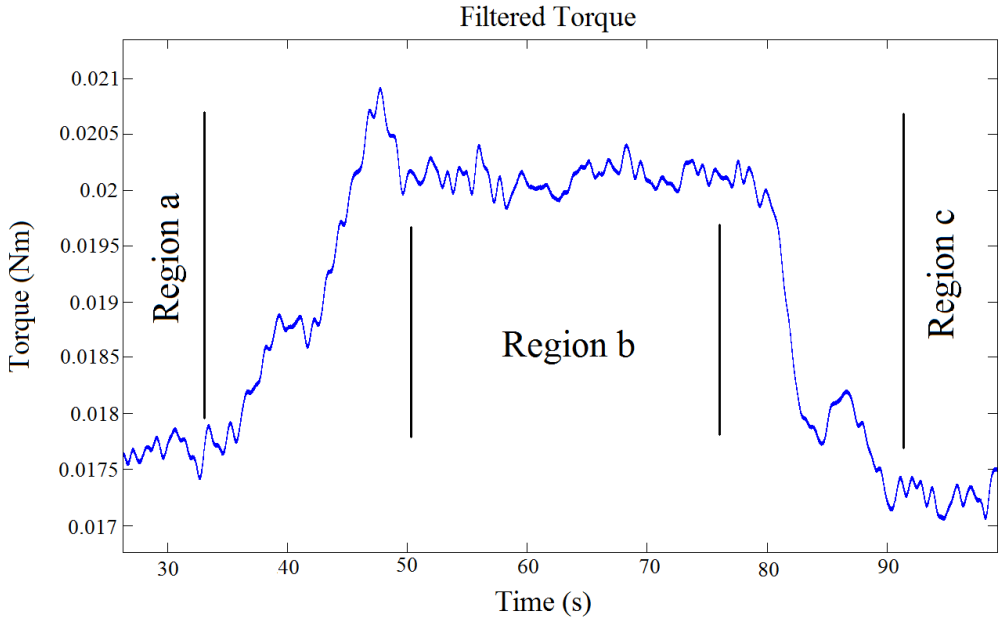

Figure 2.12 – A sample result of the torque measurement

2.5 Particle image velocimetry

Particle image velocimetry (PIV) technique was used to obtain global, quantitative flow patterns downstream the rotor and the diffuser. By using the PIV technique, 2D velocity field was recorded. The isometric view of the PIV setup for the current experiment is shown in Figure 2.13.

The PIV system consisted of the laser used to provide illumination of the tracer particles in a 2D plane, the high speed charge-coupled device (CCD) camera, and the PIV software to record the data and for post processing.

Water was seeded by Mearlin Supersparkle particles. The mean diameter of the particles was 5 – 7 μm with the relative density of 2.9 Kg/m^3. Although the density of the particles is higher than the water density, the water velocity was high enough to keep them buoyant in the flow during the experiment. The corresponding Stokes number was equal to 0.3E-03.

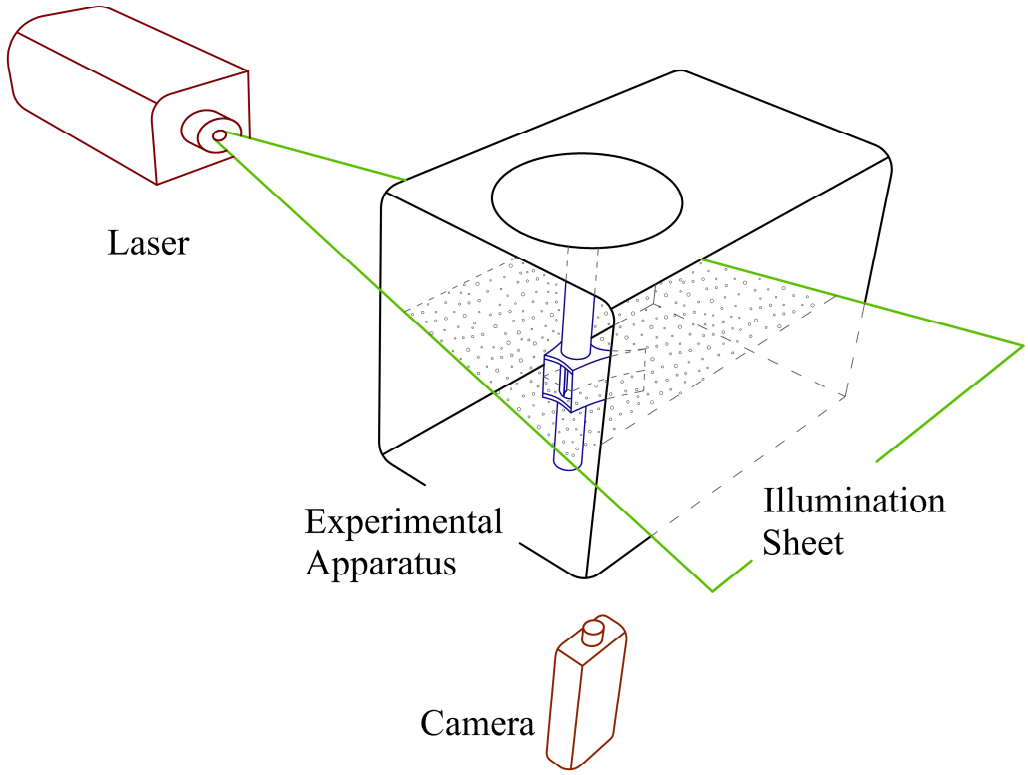

Figure 2.13 – 3D schematic of the PIV system

The laser light sheet was generated by a dual diode-pumped laser (Darvin-Duo series by Quatronix) and the images was captured by 1024 by 1024 pixels CCD camera. The images were processed by the LaVision DaVis 7.2 software.

In order to calculate the velocity field behind the rotor, a static mask was applied to each image to subtract the stationary parts of each image. Figure 2.14 (a) presents a raw PIV image from the experimental apparatus with the illuminated seeding particles for the rotor with diffuser. Figure 2.14 (b) presents the mask that was used to subtract the rotor and diffuser form the image. The raw PIV image for the rotor without diffuser is presented in Figure 2.15.

Although the mask option was used primarily to subtract the rotor and diffuser from the raw images, there were some shadow regions that were also included in the mask region. The shadow region was indicated in Figure 2.14 (b).

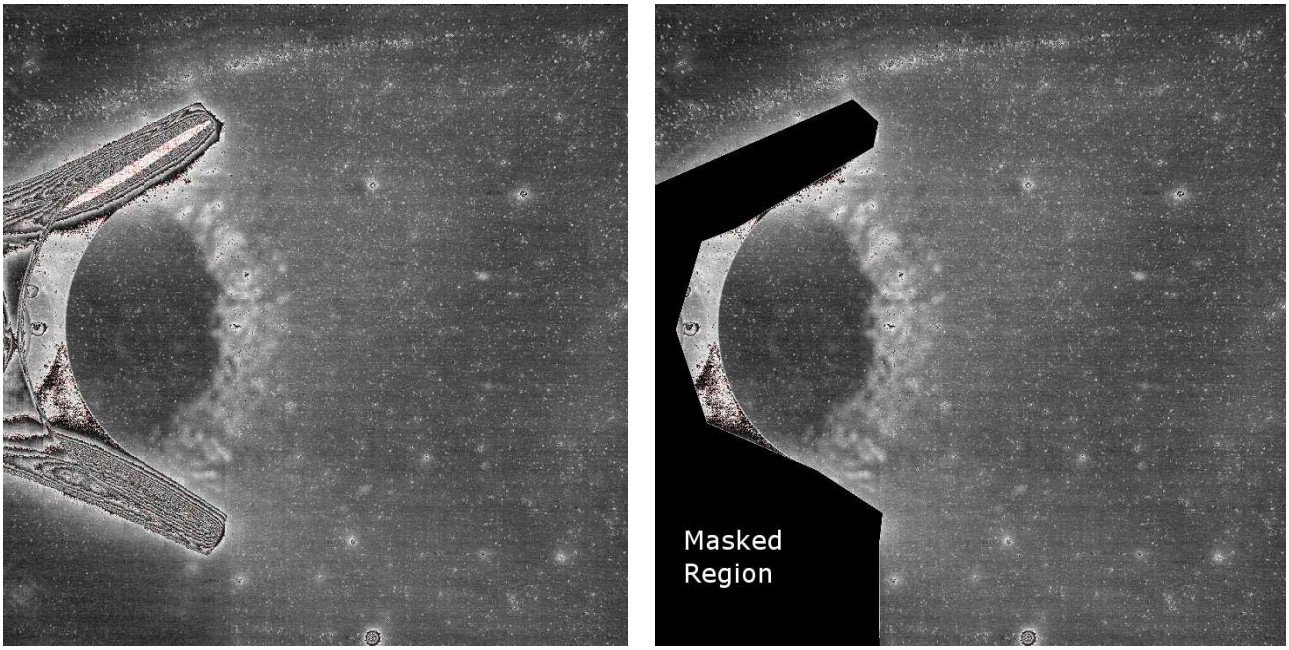

(a) (b)

Figure 2.14 – The raw PIV images from the experimental apparatus, turbine with diffuser, a) without the mask defined b) with the mask defined

Figure 2.15 – The raw PIV image of the rotor without diffuser

To calculate the velocity vector field, 16 x 16 pixel interrogation windows with 50% overlap between the windows were used. The velocity vectors were calculated by cross-correlation method and the vector loss due to filtering out of the spurious vectors inside the field was less than 1%. The resulting spatial resolution of the velocity vector field was 1.33 vectors/mm for the rotor without diffuser, and 0.9 vectors/mm for the rotor with diffuser. The total error of the calculated velocity was less than 2 %. Figure 2.16 presents the velocity vector field corresponding to the image of Figure 2.14.

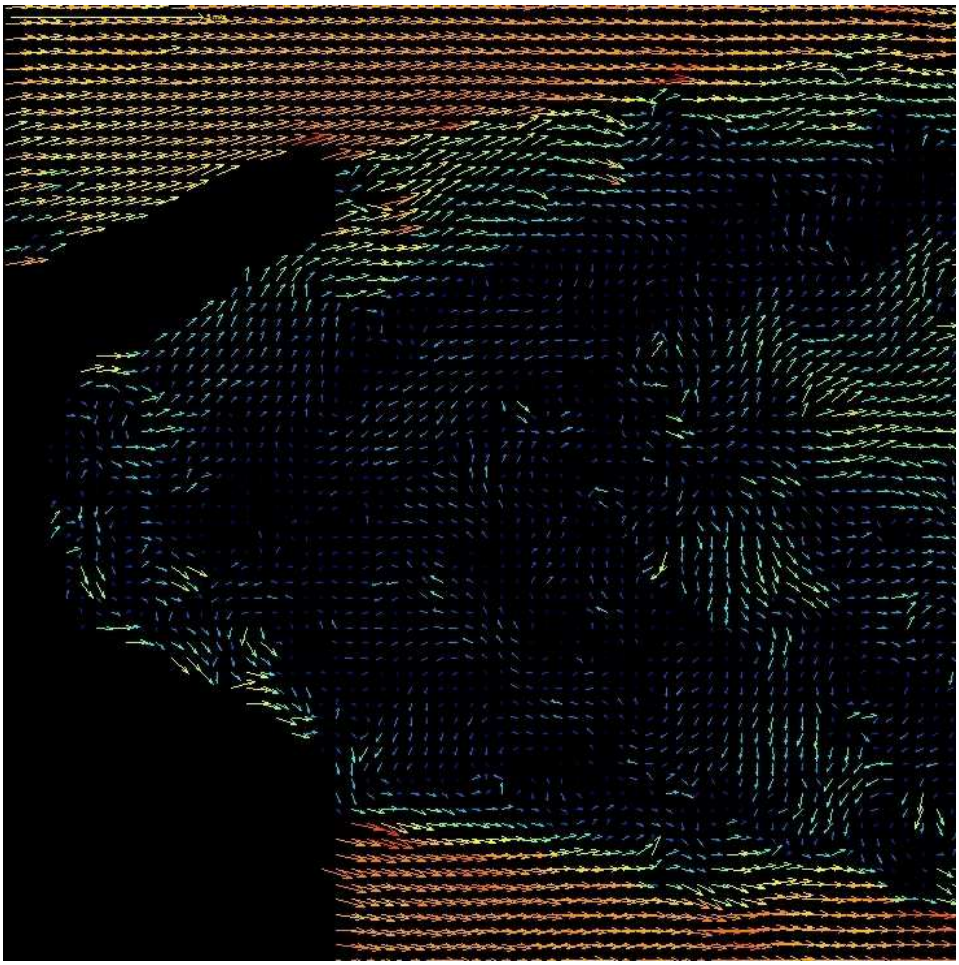

Figure 2.16 – The velocity vector field behind the diffuser calculated by the LaVision DaVis 7.2 software

CHAPTER 3

Results and discussion

3.1 Power output of turbine

The power output of a wind turbine is calculated by using the following equation:

$$P = {}^{1}/_{2}C_{p}\rho AU^{3}, \tag{3.1}$$

where C_p is the power coefficient, ρ is the air density, A is the swept area, and U is the inflow velocity. The power coefficient is defined as the ratio of the output power over the available power in the air that is passing through the turbine.

$$C_p = \frac{\text{Power}}{{}^{1}/_{2}\rho AU^{3}} \tag{3.2}$$

The swept area, A, is defined as the frontal area of the rotor which passes the air through to generate the power. Therefore, for a vertical axis wind turbine (VAWT), the swept area is the height of the rotor multiplied by the rotor diameter. In (Bouhadji and Oshkai [35]), by optimizing the position of the diffuser around the rotor, it was shown that the power output of the turbine is a function of the entrance area of the diffuser, rather than the projected frontal area of the rotor. Hence, in the current study, the swept area of the diffuser-augmented VAWT was represented by an entrance area of the

diffuser. It should be noted that the effective swept area is related to the positions of the stagnation points on the rounded leading edges of the diffuser. In the current experiment, the positions of the stagnation points, and consequently the effective swept area of the rotor, were considered to be constant, due to the small radius of the leading adges of the diffuser. As the experiments were performed in the water tunnel, the air density and the air velocity in equation (3.1) were replaced by the water density and the inflow velocity of the water respectively.

Traditionally, the performance of a wind turbine is represented by the power coefficient as a function of the tip-speed ratio. Since the power coefficient and tip-speed ratio are non-dimensional numbers, the performance curves allow comparison of turbines of different size and similar type. Also, while it is not possible to match the Reynolds number of the scaled model to that of the full-scale turbine, the kinematic similarity is obtained by matching the tip-speed ratios. Therefore, the performance of the full-size turbine can be calculated using the non-dimensional curves of the experimental results of the scaled model inside the water tunnel.

As it was discussed in section 2.4, the direct torque measurements were performed using a loadcell. The presence of rotating parts in the system introduced an error in torque measurements. In order to correct for this error, the differences between torque values was calculated when the water pump was turned on and off, as it was shown in Figure 2.12. By taking a difference of those two measurements, the residual torque in the system was calculated. The final value of the torque value was calculated by subtracting the residual torque in the system. The torque signal was digitally filtered

using the MATLAB software. Since a constant torque was expected to be imposed by the water on the rotor, a low pass filter was used to filter out the high frequencies of the results. The threshold of the filtering frequency was calculated from the rotating frequency of the electric motor. Therefore, for each test, a low pass filter was used to cut the frequencies higher than the rotating frequency. The filtering process was performed separately for each region indicated in Figure 2.12 (a sample result), to decrease the affect of signal level variation. The noise level of the system was kept lower than 10% of the measured torque.

As it was mentioned in chapter 2, each data set was obtained by varying the rotational speed of the turbine at a constant inflow velocity to obtain the torque as a function of rotational speed. After that, the torque was converted to the power using the following equation

$$P = T \cdot \omega, \tag{3.3}$$

where T is the torque magnitude (Nm), and ω is the rotational speed (rad/sec). With the power calculated from equation 3.3, the power coefficient was obtained from equation 3.2.

The water velocity in the tunnel was measured by the frequency of rotation of the water pump. A calibration curve was used to convert the pump frequency (1/s) to the water velocity (m/s) for different water depth in the tunnel. In the current experiment, the calibration was also performed by PIV technique to obtain the flow velocity for specific experimental conditions.

Since the experimental hardware inside the water tunnel blocked a portion of the tunnel cross section, the inflow velocity changed due to the change of the cross section area. Therefore the flow blockage by the experimental apparatus must be taken into account before the power coefficient is calculated using Eqn. 3.2. There are two sources of flow blockage in the current experiment. The first one is the blockage by a rotating object (the turbine rotor). The second source is the blockage by the stationary parts of the experimental apparatus. Okajima et al [36] suggested that the velocity corrections for stationary parts should be taken into account for a blockage ratios higher than 5%. Also, Norberg [37] did not use corrections for the blockage ratio of 5%. For the current study, the corrections for the cylindrical support sleeves and the diffuser were neglected due to the relatively low blockage ratio of them, which was equal to 6%.

Furthermore, Advisory Group for Aerospace Research & Development (AGARD) [38] suggested that for the wind tunnel applications, rotating objects have more significant effect on the velocity than the stationary parts.

The rotation of the turbine rotor induces changes in the flow velocity in the water tunnel. Therefore, the blockage correction due to the presence of the rotor is essential in order to obtain correct values of the power coefficient. The Mikkelsen method was used to study the blockage correction for the current design [39, 40]. The blockage ratio of the rotor was 1.6% of the water tunnel cross section area. Figure 3.1 presents the variation of V_c/V_{inf} as a function of Cp, where V_c is the corrected velocity by using Mikkelsen method and V_{inf} is the inflow velocity.

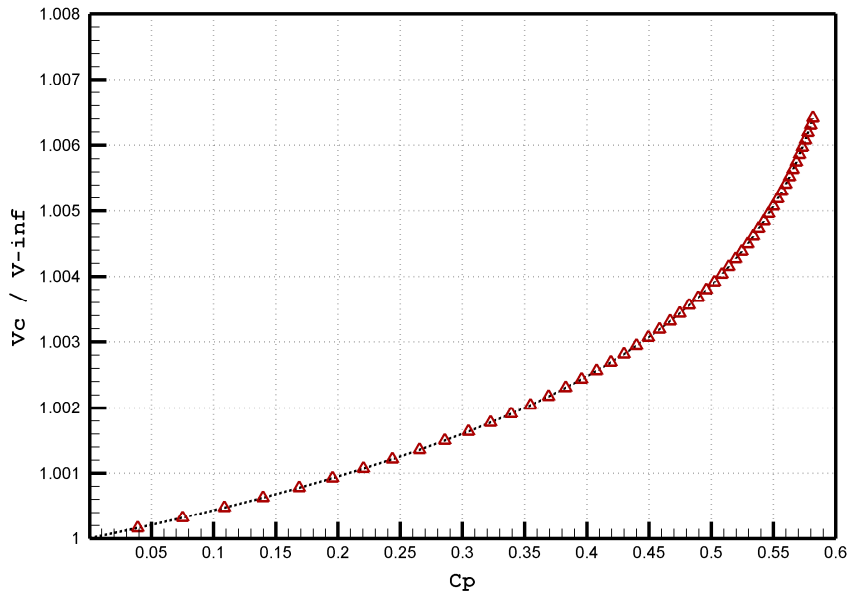

Figure 3.1 – The ratio of corrected velocity and the inflow velocity versus the power coefficient

From Figure 3.1, one can see that the correction for the current experiment is less than 1% for the power coefficients below the Betz limit (Cp=0.59). Since the power coefficient of the conventional VAWTs (without diffuser) is less than 35% [41], the corresponding correction for the velocity magnitude is less than 0.2%.

The velocities of 0.451, 0.533, 0.615 and 0.697 m/s were considered in the current study. For the velocities lower than 0.451 m/s, the torque output of the turbine was not high enough to obtain enough points to plot the performance curves. Also at velocities higher than 0.697 m/s, undesired air bubbles were generated from the cylinder sleeves downstream of the rotor.

3.2 The performance of the turbine without diffuser

In Figure 3.2, the power output of the turbine without diffuser is presented for different water velocities as a function of the tip-speed ratio. Each data point in the plots was obtained by calculating the output torque of the system which was converted to the power using equation 3.3. The range of tip-speed ratio was chosen between 0.1 and 1.15 to observe the maximum value of the power coefficient. The maximum power output for the inflow velocities of 0.451, 0.533, 0.615 and 0.697 m/s was at the tip-speed ratios of 0.63, 0.67, 0.68 and 0.71, respectively.

In Figure 3.3, the power coefficient curves are plotted versus the tip-speed ratio for different water velocities. The values were calculated using equation 3.3. By definition, the power coefficient is the ratio of the power output over the maximum power that can be extracted form the flow. Hence, the Cp curves in Figure 3.3 represent the efficiency of the turbine at different tip-speed ratios. According to the Cp plots, the maximum Cp of 0.26 was observed at the inflow velocity of 0.533 m/s and the tip-speed ratio of 0.67. The current rotor design utilized both the lift and the drag components of the force acting on each blade to produce the rotation. Since the lift force increases with the increase of the Reynolds number, a corresponding increase in Cp is expected. This trend is observed in Figure 3.3, which shows that the Cp increases with the increase in the inflow velociry. The combined scatter plot of all data points shown in Figure 3.3 is presented in Figure 3.4.

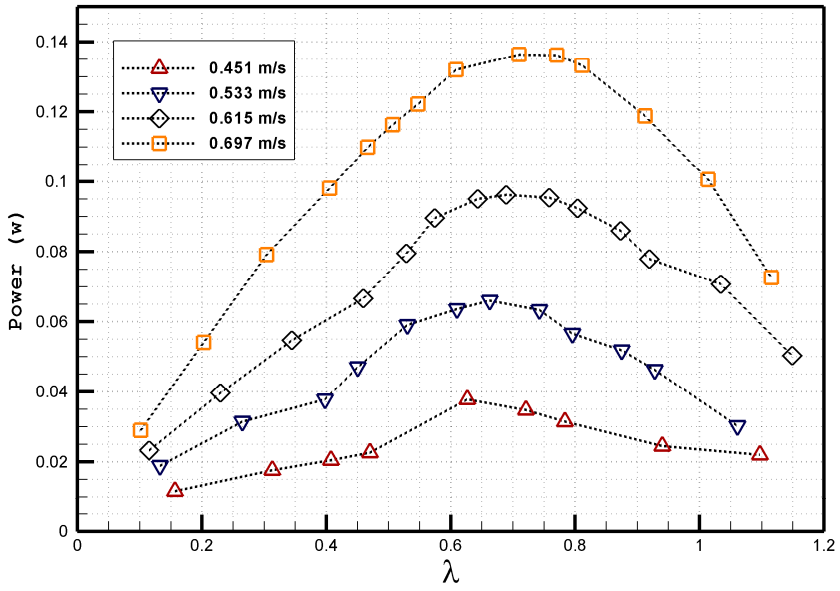

Figure 3.2 – The power output of the turbine without diffuser versus the tip-speed ratio

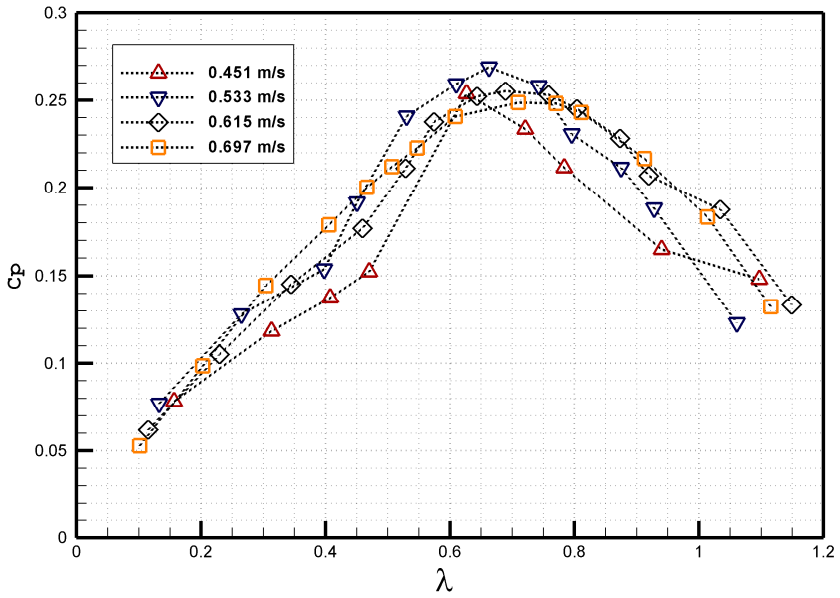

Figure 3.3 – The power coefficient of the turbine without diffuser versus the tip-speed ratio

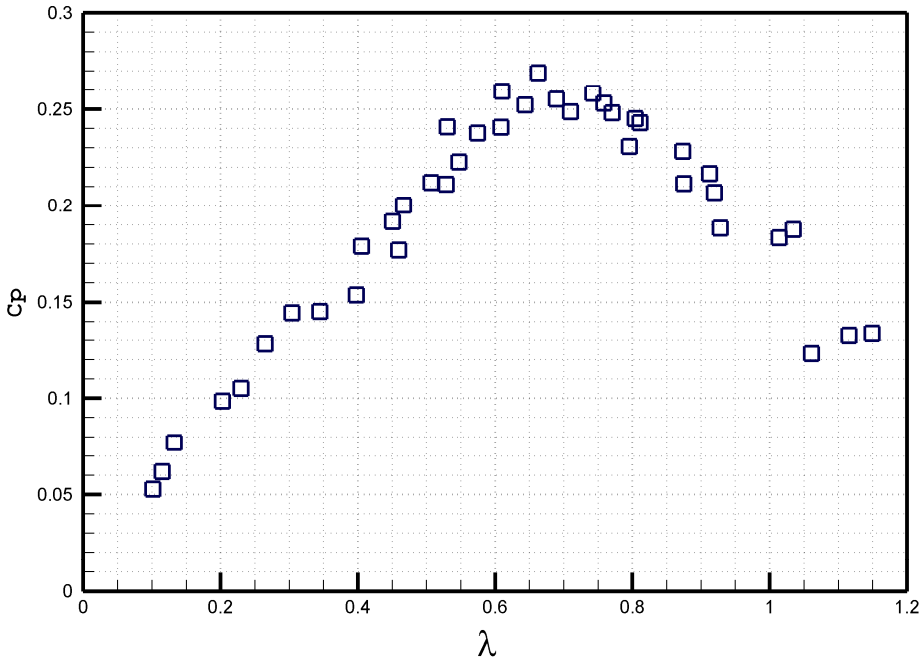

Figure 3.4 – The scatter plot of the power coefficient of the turbine without diffuser versus the tip-speed ratio

3.3 The performance of the turbine with diffuser at zero angle of attack

The power output of the turbine as a function of the tip-speed ratio with the diffuser around the rotor is illustrated in Figure 3.5. The power output was calculated by using the method presented in the previous section, i.e. using equation 3.3. In this set of tests, the tip-speed ratio was changed from 0.2 to 1.62. The maximum power output for the inflow velocities of 0.451, 0.533, 0.615 and 0.697 m/s was observed at the tip-speed ratios of 1.25, 1.2, 1.26 and 1.26, respectively.

The Cp curves as functions of tip-speed ratio are plotted in Figure 3.6 for four different inflow velocities. Similar to the previous section, each point was calculated using equation 3.2. In accordance with Figure 3.6, the maximum Cp was 0.355 for the 0.697 m/s water velocity and the tip-speed ratio of 1.26. Finally, the scatter plot of all the four curves in Figure 3.66 is presented in Figure 3.7.

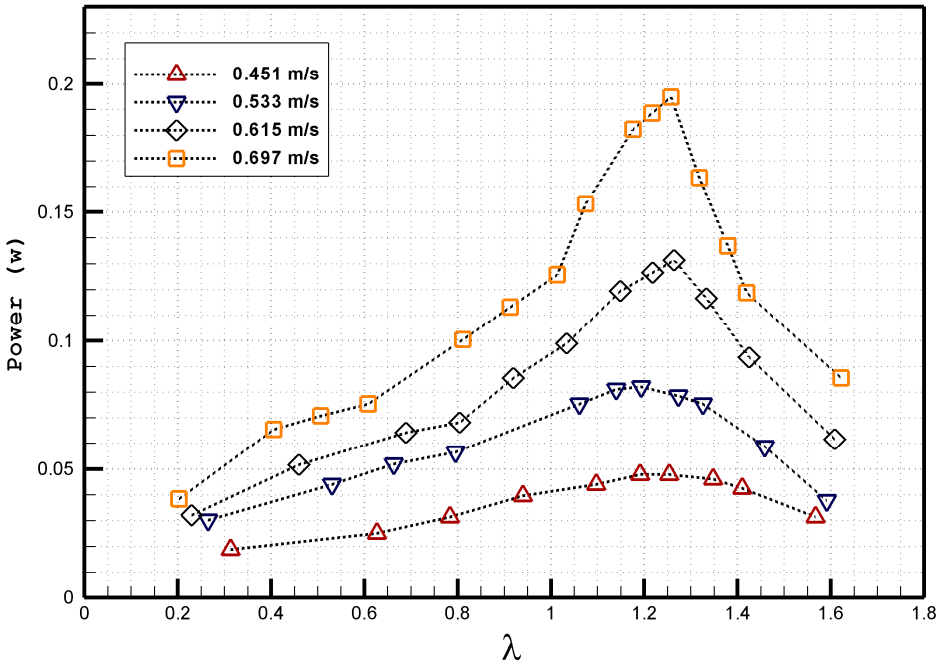

Figure 3.5 – The power output of the turbine with diffuser versus the tip-speed ratio

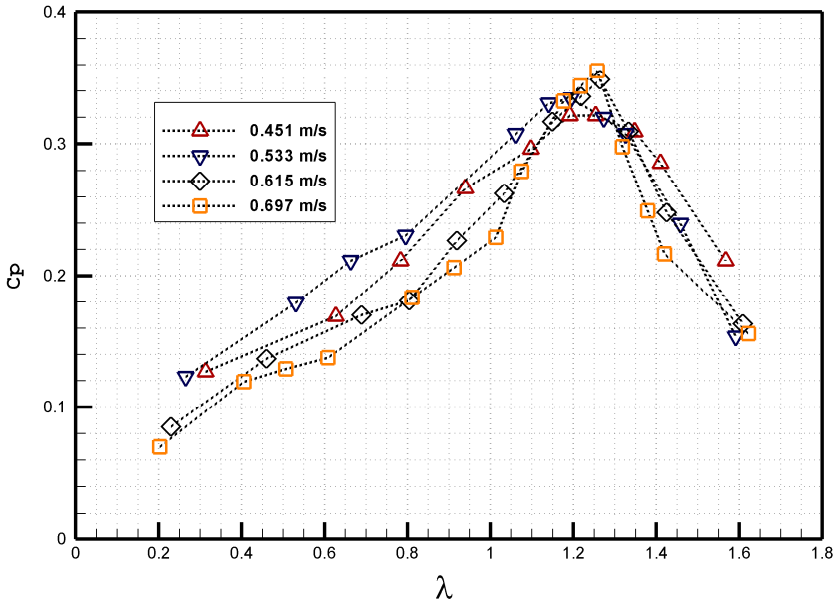

Figure 3.6 – The power coefficient of the turbine with diffuser versus the tip-speed ratio

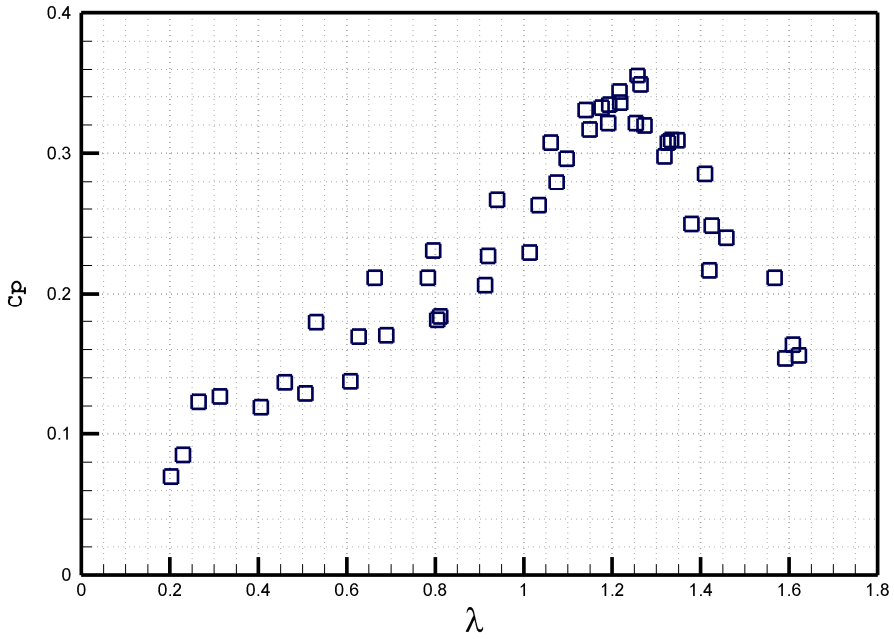

Figure 3.7 – The scatter plot of the power coefficient of the turbine with diffuser versus the tip-speed ratio

3.4 Time-averaged flow patterns

3.4.1 Background

Understanding the flow patterns inside and downstream the rotor can lead to improved methods for prediction of power output of wind turbines. In particular, there exist several theoretical methods for prediction of the power output of a VAWT that are based on the knowledge of the velocity field around the rotor [6, 42]. The momentum models can be classified as the single streamtube model [43], the multiple streamtube model [44], and the double-multiple streamtube model [45, 46]. Furthermore, other methods are suggested to calculate the power output based on the knowledge of the vortex shedding of each blade in one complete rotation. Therefore, the velocity field inside the rotor and downstream of the rotor can be used to calculate the vortex shedding from the blades [6, 47]. Furthermore, the velocity field inside the rotor can be used to optimize the blade design.

In the present study, particle image velocimetry (PIV) was used to visualize the flow pattern and the wake structure of the turbine with and without a diffuser. By using the PIV technique, the flow structure downstream of the turbine can be studied and the influence of the diffuser on the wake can be visualized.

Although in the current study the rotor and diffuser were made from a transparent material, the region of the flow inside the rotor was optically inaccessible due to

parallax effects. On the other hand, the flow pattern inside the diffuser could be recorded.

The vorticity contours, the streamlines, and the velocity contours in the wake of the turbine are presented for two different configurations: with and without the diffuser. The out-of-plane vorticity, ω_z, was calculated numerically from the PIV velocity vector fields using the following equation.

$$\omega_z = \frac{\partial v}{\partial x} - \frac{\partial u}{\partial y} \tag{3.4}$$

where u and v are the x- and the y-components of velocity, respectively. The vorticity magnitude, the streamlines, and the velocity contours were plotted using the Tecplot software.

The time-averaged velocity fields, which were used to illustrate the steady flow patterns, were generated from the time-averaged vectors exported from a sequence of instantaneous PIV images. The number of images used to calculate the time-averaged velocity field was chosen to be between 60 and 70 images.

3.4.2 Time-averaged flow patterns downstream of the turbine without diffuser

The time-averaged flow patterns downstream of the turbine without diffuser are presented in Figures 3.8 and 3.9. The PIV images were recorded in a 2D plane at the center of the rotor, perpendicular to the axis of rotation. The direction of rotation of the

rotor in all of the images is clockwise and the flow direction is from left to right. Six different tip-speed ratios were considered in order to study the wake pattern downstream of the rotor. These tip-speed ratios are 0.3, 0.45, 0.6, 0.8, 1.0 and 1.15. These values correspond to the range of tip-speed ratios presented in Figure 3.3.

Figure 3.8((a) to (f)) presents the out-of-plane vorticity contours of the wake region downstream of the rotor. Figure 3.9((a) to (f)) presents the corresponding streamlines superimposed on the velocity contours. Some of the vortices in Figure 3.9((a) to (f)) were labelled to simplify the discussion. For each label, the subscript refers to the specific plot, in which the label is used.

As it is shown in Figure 3.8((a) to (f)), two shear layers existed downstream of the rotor. The shear layer at the top of the plot consisted of negative (clockwise) out-of-plane vorticity, and the lower shear layer consisted of positive (counter clockwise) out-of-plane vorticity.

Similarly to the maximum values of vorticity magnitude (Figure 3.8(a) to (f)), the inclination angle of top shear layer with respect to the inflow direction decreases when the tip-speed ratio increases. The angle between the top layer and the horizontal (streamwise) direction is approximately +5° at $\lambda = 0.3$. This value decreases to 0°, -5°, -10°, -15°, and -20° for $\lambda = 0.45$, 0.6, 0.8, 1.0, and 1.15, respectively. This decrease is caused by the change of the wake flow direction with the change of the tip-speed ratio. In contrast, the angle of lower shear layer does not change when the tip-speed ratio increases. This shear layer has the inclination angle of -5° with respect to the horizontal direction.

The vorticity contours show that the range of vorticity magnitude as a function of tip-speed ratio was increased slightly from +/- 0.05 1/s to +/- 0.06 1/s while λ increased. The highest vorticity magnitudes (0.05 and -0.05 1/s) were observed at λ = 0.3.

An additional insight into the vortical structure of the wake can be obtained from the streamline plots (Figure 3.9). Figure 3.9(a) shows a large-scale vortex located at x/D= 1.5 (vortex A_a). This vortex blocked the flow passing through the rotor. Therefore, a large portion of the fast-moving flow changed direction and resulted in a large wake at λ = 0.3. This vortical structure (vortex A_a) will be referred to as a blockage vortex.

The blockage vortex moved from x/D= 1.5 to x/D= 2 when the tip-speed ratio changed from λ = 0.3 to λ = 0.45 (vortex A_b Figure 3.9(b)). The blockage effect of the vortices downstream of the rotor starts to diminish with the increase of the tip-speed ratio. Formation of elongated positive and negative vortices downstream of the rotor indicates the dissipation of the blockage vortices and formation of well- defined shear layers downstream of the rotor (Figure 3.8(c) to (f)).

In Figure 3.8, one can see highest vorticity magnitudes distributed along the shear layers. These high values of vorticity correspond to significant flow fluctuation downstream of the rotor. The vortices start to dissipate downstream of x/D = 3, 2.5 and 1.5 for λ = 0.8, 1.0 and 1.15.

As it was mentioned above, at low tip-speed ratios, the blockage vortices (A_a and A_b in Figure 3.9(a) and (b), respectively) interfered with the flow passing through the

rotor. When the tip-speed ratio increased (Figure 3.9(c) and (d)), the blockage vortices dissipated and small-scale vortices were formed. According to Figure 3.9(c), the blockage vortices (A_c and B_c) convected farther downstream. This change in the wake structure corresponded to the increase in the power coefficient (Figure 3.3). Figure 3.9(d) shows that small-scale vortices (A_d, B_d, C_d, and D_d) formed at x/D = 1, 1.6, 1.8 and 2 at the tip-speed ratio of 0.8.

Figures 3.9(e) and (f) present the streamlines and the velocity contours of the flow downstream of the rotor for tip-speed ratios of 1.0 and 1.15. A recirculation region formed in the wake and interfered with the flow passing through the rotor (region A_e in Figure 3.9(e) and region A_f in Figure 3.8(f)). This flow pattern is due to the high pressure drop in the wake that existed for the high tip-speed ratios. Development of this flow structure corresponds to the decrease of the power output shown in Figure 3.2.

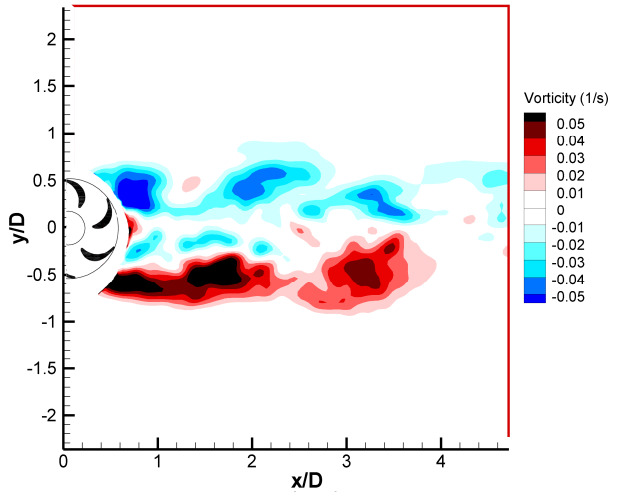

a) λ = 0.3

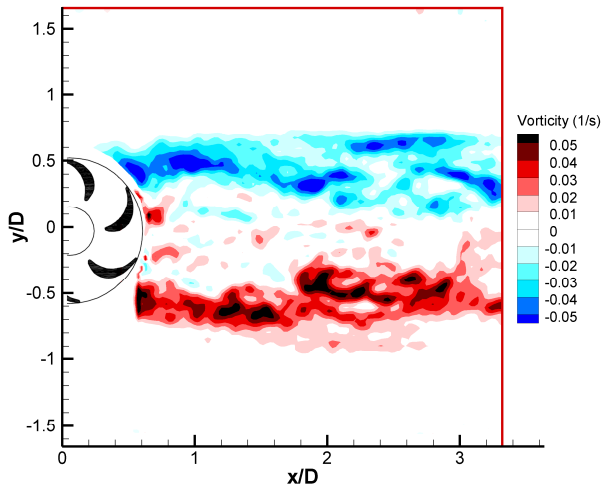

b) λ = 0.45

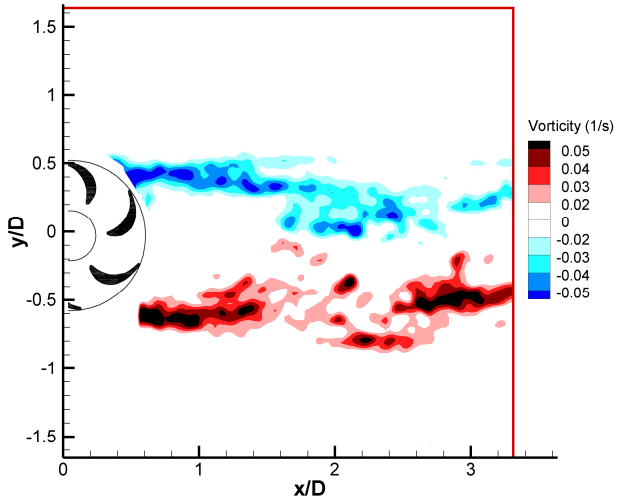

c) λ = 0.6

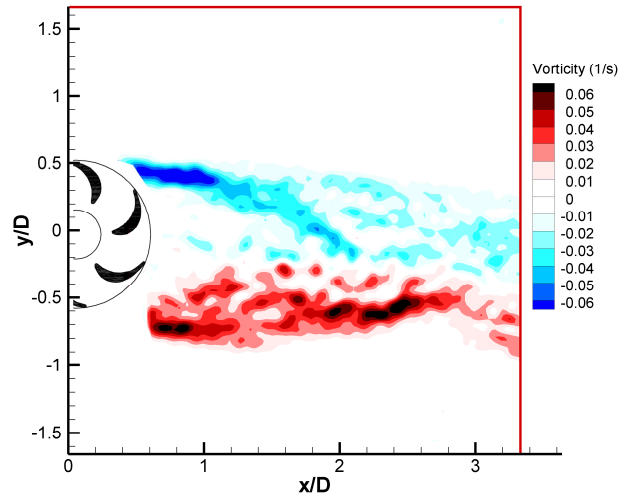

d) λ = 0.8

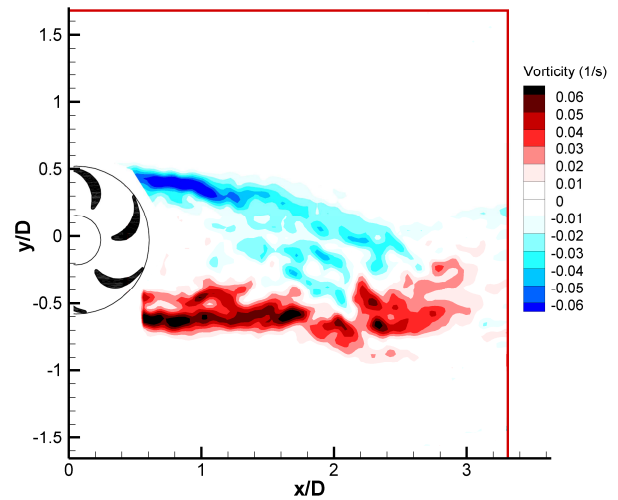

e) λ = 1.0

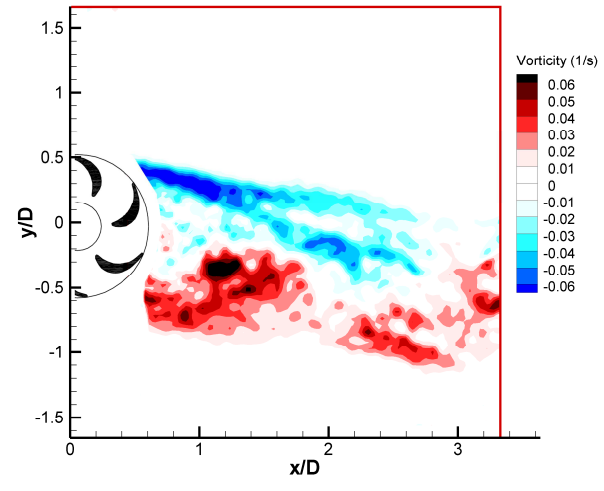

f) λ = 1.15.

Figure 3.8 – Time-averaged out-of-plane vorticity contours downstream of the rotor without diffuser at tip-speed ratios of **a)** λ=0.3, **b)** λ=0.45, **c)** λ=0.6, **d)** λ=0.8, **e)** λ=1.0 and **f)** λ=1.15. The rotation direction is clockwise and the flow direction is from left to right.

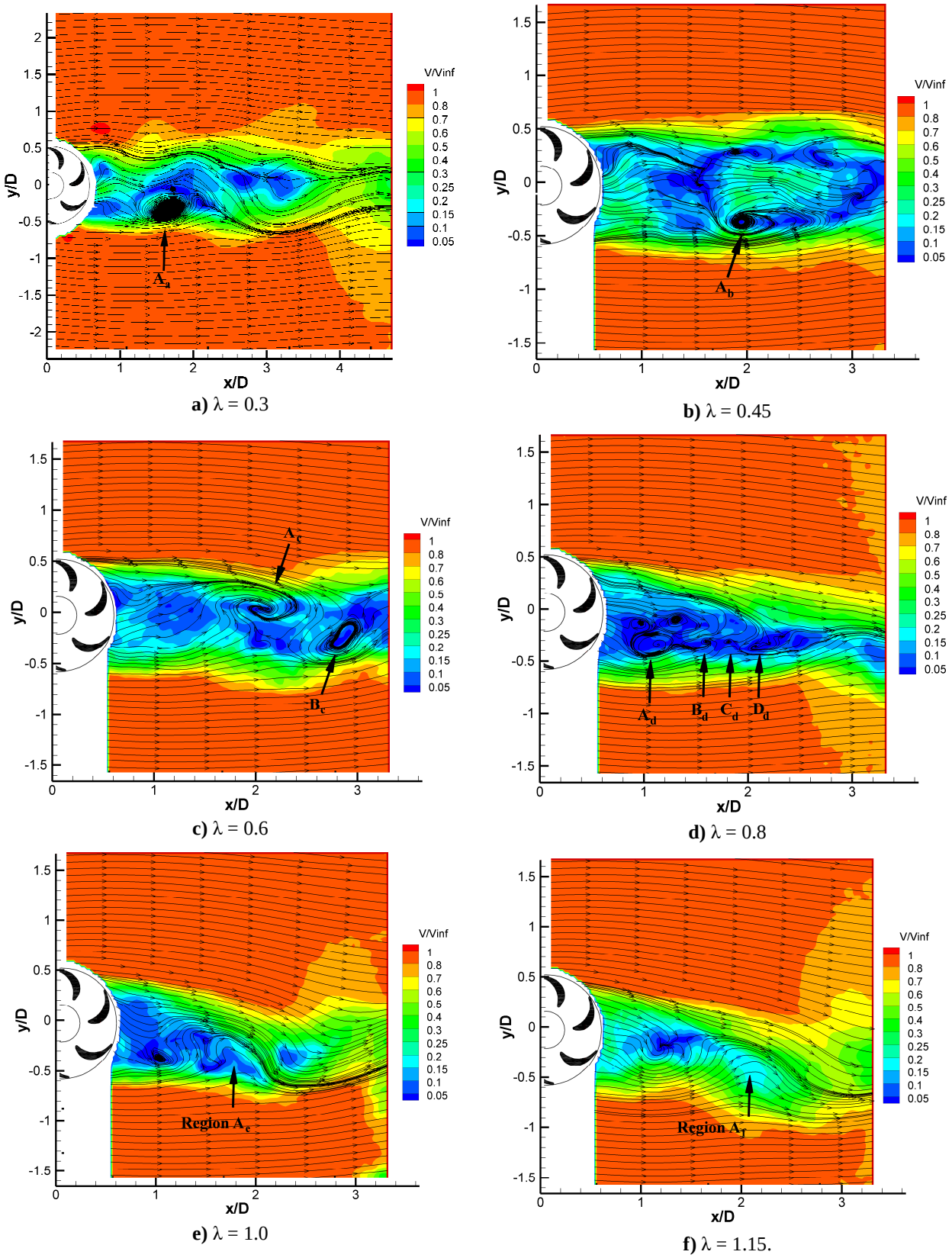

a) λ = 0.3

b) λ = 0.45

c) λ = 0.6

d) λ = 0.8

e) λ = 1.0

f) λ = 1.15.

Figure 3.9 – Time-averaged streamlines and velocity contours downstream of the rotor without diffuser at tip-speed ratios of a) λ=0.3, b) λ=0.45, c) λ=0.6, d) λ=0.8, e) λ=1.0 and f) λ=1.15. The rotation direction is clockwise and the flow direction is from left to right for each image.

3.4.3 Time-averaged flow patterns downstream of the turbine with diffuser

Figures 3.10((a) to (f)) and 3.11((a) to (f)) illustrate the time-averaged flow patterns downstream of the rotor of the turbine with the diffuser. The PIV technique, which was described in Section 2.5, was used for flow visualization. The field of view was the same as in the previous section, i.e. along a 2D plane at the center of the rotor, perpendicular to the axis of rotation. The direction of rotation of the rotor is clockwise in all the images with the flow passing through the rotor from left to right. Six different tip-speed ratios were studied through the images to investigate the wake pattern downstream of the rotor and the diffuser. The value of tip-speed ratios are 0.5, 0.6, 0.8, 1.15, 1.3 and 1.6. These values correspond to the range of tip-speed ratios presented in Figure 3.6.

Figure 3.10((a) to (f)), show the out-of-plane vorticity contours of the wake region downstream of the rotor. Since the diffuser was made of WaterShed material, it was possible to obtain the velocity field inside the diffuser. The contour lines in Figure 3.10 represent the magnitude and the size of vortices with the out-of-plane vorticity magnitude for a specified range.

The corresponding streamlines superimposed on the velocity contours of the wake region downstream of the rotor are illustrated in Figure 3.11((a) to (f)). all of the Figures 3.10((a) to (f)) and 3.11((a) to (f)) have the same range of tip-speed ratios. Similarly to the previous section, some vortices were labelled for simplification of the

discussion. The subscript of each label of the vortices indicates the sub image of Figure 3.11((a) to (f)).

The vorticity plots in Figure 3.10((a) to (f)) confirm the formation of four shear layers downstream of the rotor and diffuser. Two of the shear layers were formed at the trailing edge of the diffuser and the other two were formed at the rotor inside the diffuser. The shear layers at the top of the plot consisted of negative (clockwise) vortices, and the lower shear layers consisted of positive (counter clockwise) vortices.

The comparison between the sub images of Figure 3.10((a) to (f)) shows that the wake region is approximately symmetric with respect to the center line of the rotor. Also, the shear layers downstream of the rotor were attached to the diffuser shear layers downstream of the diffuser.

The location where the top shear layers that originated from the diffuser and from the rotor merge located at x/D=3.5 for λ = 0.5, 0.6, 1.15, and 1.3. For λ = 0.8 and 1.6 the top shear layers form the diffuser and the rotor merge at x/D=2.5.

The location where the lower shear layers that originated from the diffuser and from the rotor merge located at x/D=2.5 for λ = 0.5, 0.8, 1.15 and 1.3. For λ = 0.6 and 1.6 the lower shear layers form the diffuser and the rotor merge at x/D=3.5.

In accordance with Figure 3.10((a) to (f)), the angle between the top layer and the horizontal (streamwise) direction is +15° for all of the tip-speed ratios. This angle is also -15° for the lower shear layers downstream of the diffuse. Therefore the shear layers of the diffuser are symmetrical along the horizontal (streamwise) center line of the diffuser.

The angle between the horizontal (streamwise) direction and the rotor shear layers downstream of the rotor also are almost the same for all the tip-speed ratios. The angles are between +35° and +30° for the top layers and -30° for the lower ones. This angle at the reattachment point is +30° at top of the plots and -30° at bottom of the plots for all of the tip-speed ratios.

The range of vorticity magnitude is +/- 0.05 (1/s) for most of the tip-speed ratios except for $\lambda = 0.5$ and $\lambda = 1.6$, which the range is +/- 0.04 (1/s) and +/- 0.06 (1/s) respectively. The highest vorticity magnitudes were at the shear layers for all the tip-speed ratios, although there are some high-circulation vortices in the wake region due to the highly turbulent flow downstream of the diffuser.

The shear layers downstream of diffuser along the tip of the diffuser profile have lower magnitude than the shear layers downstream of the rotor at the top of the plots; on the other hand, the lower shear layers downstream of diffuser have the highest magnitude due to the rotating direction of the rotor.

The stream lines of the flow in Figure 3.11((a) to (f)) present an illustration of the vortical structure in the wake region downstream of the rotor. From each sub images of Figure 3.11((a) to (f)), one can see the low-velocity backward (recirculating) flow in the wake region. The backward flow is the result of high pressure drop of the flow at the exit section of the diffuser. The backward flow starts to dissipate from x/D=3 to 4 for all the tip-speed ratios. Moreover, for all of the tip-speed ratios, presented in Figure 3.11((a) to (f)), the flow direction reverts to the forward one at x/D=4.

The blockage vortices downstream of the rotor with the diffuser are generally larger than the blockage vortices shown Figure 3.9((a) to (f)). Figure 3.11(a) shows three blockage vortices downstream of the rotor at x/D=1.5, 2 and about 3 (A_a, B_a, and C_a) for $\lambda = 0.5$. The blockage vortices start to dissipate when the tip-speed ratio increases to 1.15. For $\lambda = 1.15$ (Figure 3.11(d)), one can see the formation of small-scale vortices which were shed form the rotor. Figure 3.11(e) presents the stream lines at $\lambda = 1.3$ which corresponded to the peak of the power coefficient (Figure 3.6).

Unlike the flow patterns of rotor without diffuser, which was discussed in the previous section, the vortex shedding from the rotor occurs both from the top and the bottom side. This characteristic of the wake region creates larger blockage vortices for the small tip-speed ratios.

While there are no vortices downstream of the rotor without diffuser at high tip-speed ratios, Figure 3.11(f) illustrates the formation of large-scale vortices downstream of the rotor with diffuser at x/D=1 and 2 for $\lambda = 1.6$. The large-scale vortices downstream of the rotor (A_f and B_f) block the flow which is passing through the rotor.

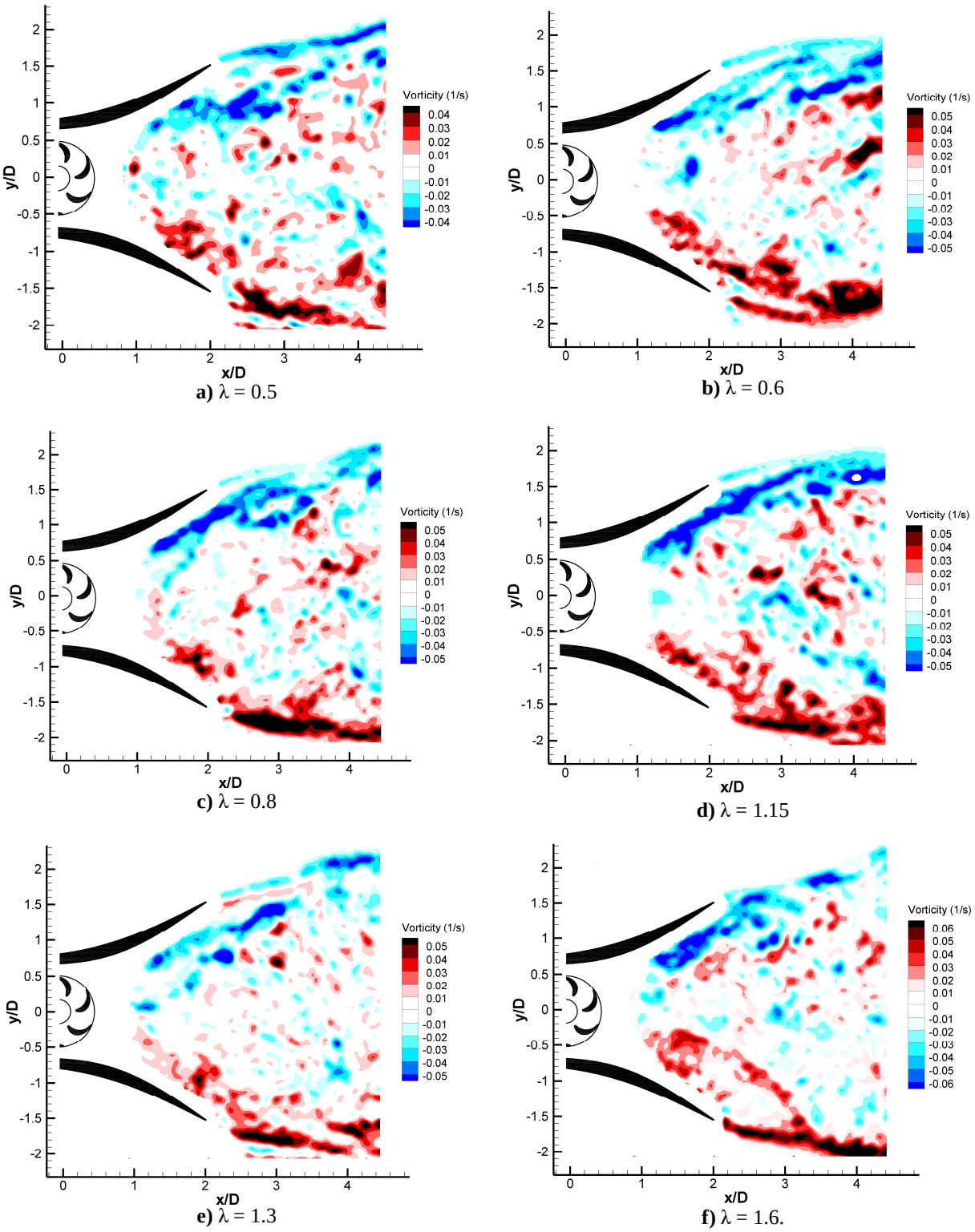

a) λ = 0.5 **b)** λ = 0.6

c) λ = 0.8 **d)** λ = 1.15

e) λ = 1.3 **f)** λ = 1.6.

Figure 3.10 – Time-averaged out-of-plane vorticity contours downstream of the rotor with diffuser at tip-speed ratios of **a)** λ=0.5, **b)** λ=0.6, **c)** λ=0.8, **d)** λ=1.15, **e)** λ=1.3 and **f)** λ=1.6. The rotation direction is clockwise and the flow direction is from left to right for each image.

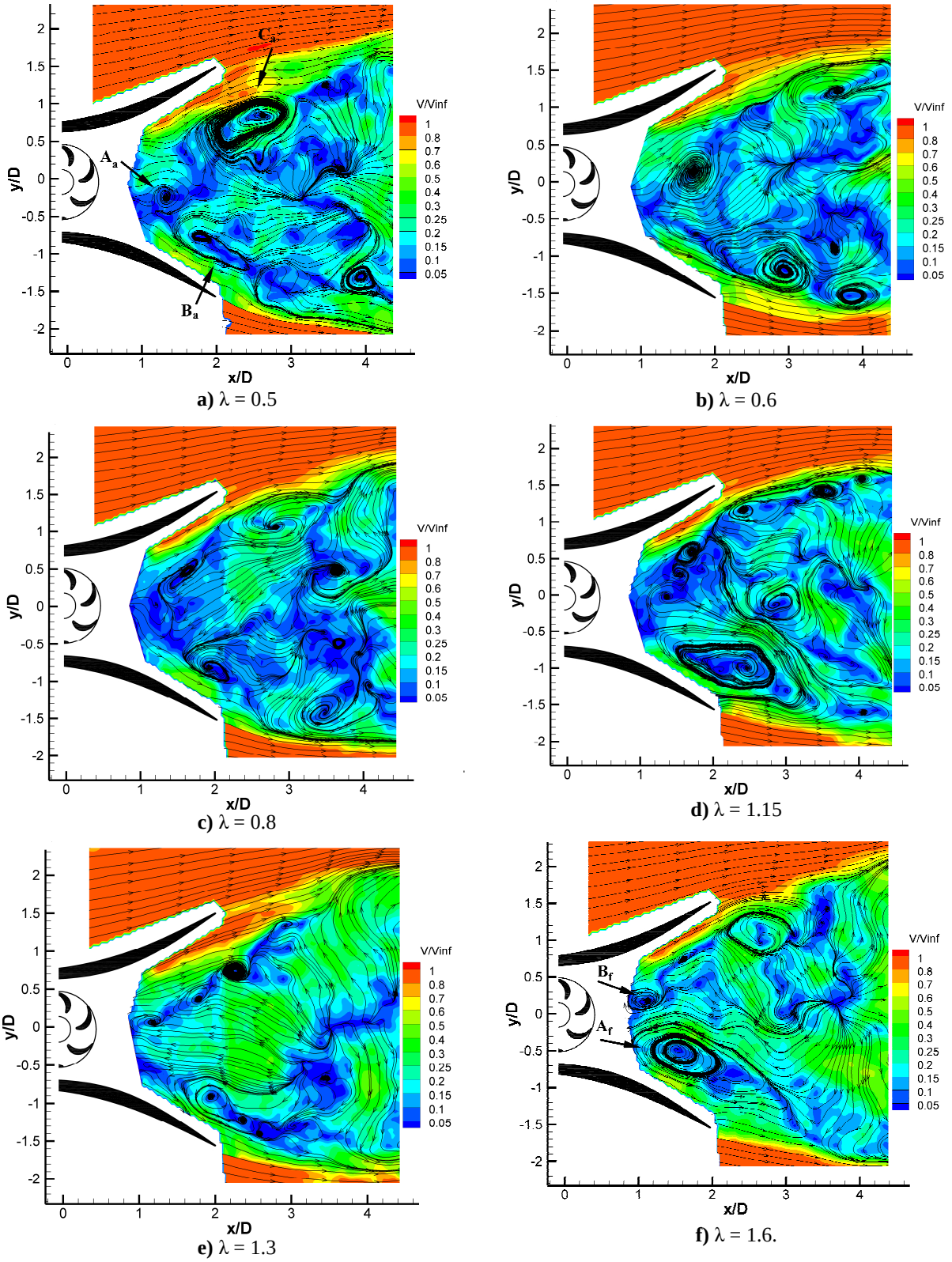

a) λ = 0.5

b) λ = 0.6

c) λ = 0.8

d) λ = 1.15

e) λ = 1.3

f) λ = 1.6.

Figure 3.11 – Time-averaged streamlines and velocity contours downstream of the rotor with diffuser at tip-speed ratios of **a)** λ=0.5, **b)** λ=0.6, **c)** λ=0.8, **d)** λ=1.15, **e)** λ=1.3 and **f)** λ=1.6. The rotation direction is clockwise and the flow direction is from left to right for each image.

3.5 Comparison and discussion of the turbine performance with and without diffuser

Figure 3.12 illustrates the power curves for the turbine *with* and *without* diffuser. The labels *"(w)"* and *"(w/o)"* in the legend of the plot correspond to the configurations *with* and *without* the diffuser, respectively. Also, identical colors for the symbols refer to identical water inflow velocity.

According to Figure 3.12, power output of the turbine when there is a diffuser around the rotor is lower than the power output of the bare rotor for the low tip speed ratios. The power output increased as the tip-speed ratio exceeded 0.8. From $\lambda = 0.8$ to $\lambda = 0.9$, the power output from the turbine with diffuser exceeded that of the turbine without diffuser. After reaching the maximum value of 0.19, 0.13, 0.08 and 0.05 (W) for the inflow velocities of 0.697, 0.615, 0.533 and 0.451 (m/s) respectively, the power output of the turbine with diffuser decreased to a value less than the maximum power output of the bare rotor at $\lambda = 1.4$.

The reason of the low power output for the turbine with diffuser at the low values of λ ($\lambda < 0.8$) can be described in terms of the effects of the blockage vortices in the wake of the rotor. As it was discussed in Section 3.4, the blockage vortices interfere with the flow downstream of the rotor. As a result, the flow is passing around the rotor instead of passing through it and interacting with the blades.

The flow pattern downstream of the rotor with diffuser was discussed in the previous section. A schematic of the blockage vortices is presented in Figure 3.13. This figure is a simplified outline of the flow streamlines at the wake region of Figure 3.11(a) for $\lambda = 0.5$.

The detailed flow pattern is shown in Figure 3.11(a). The direction of rotation of the rotor in Figure 3.13 is clockwise, and the flow is passing through the system from left to right.

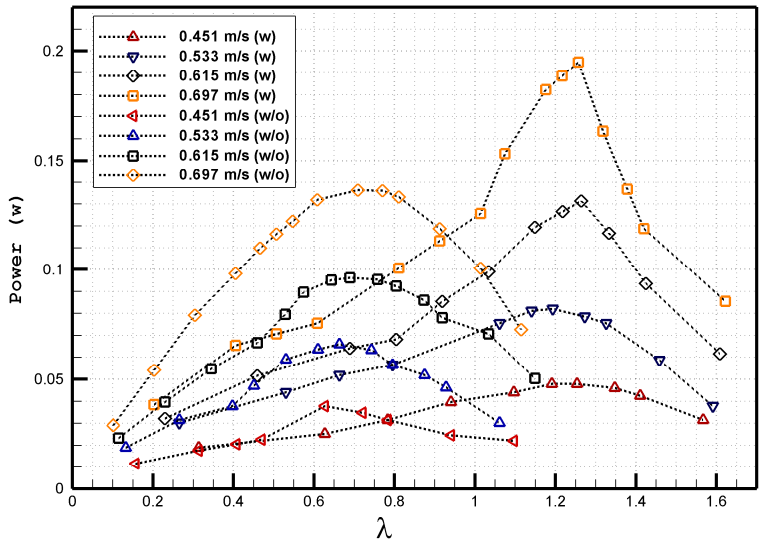

Figure 3.12 – The comparison of power output of the turbine *with* and *without* diffuser for different water velocities as a function of the tip-speed ratio

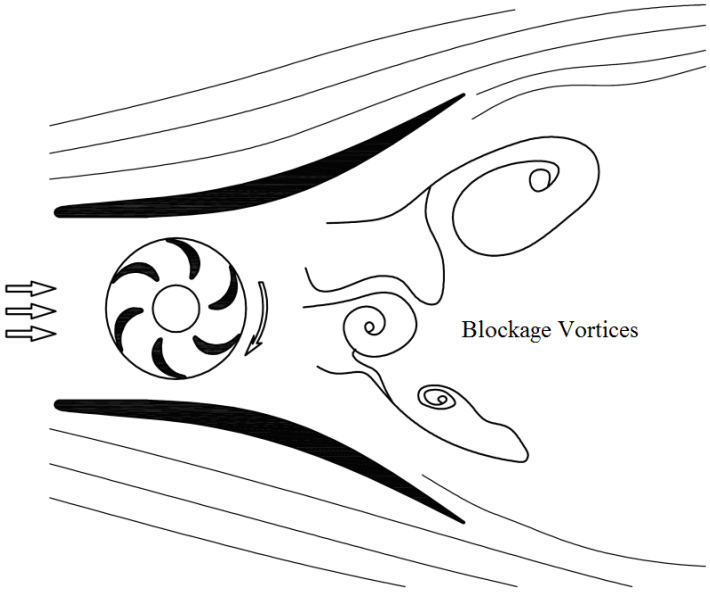

Figure 3.13 – The blockage vortices downstream of the rotor with diffuser for $\lambda = 0.45$

The maximum power output of both configurations (with and without diffuser) for different water velocities and the percentage of power increase are presented in table 3.1.

Table 3.1 - The maximum power output comparison of the turbine configurations with and without a diffuser at different water velocities

Water Velocity (m/s)	**Maximum Power Output (Nm) Without Diffuser**	**Maximum Power Output (Nm) With Diffuser**	**Maximum Power Increase (%)** (Comparison between the maximum power output for *with* and *without* diffuser configuration)
0.451	0.038	0.048	26.7
0.533	0.066	0.082	24.3
0.615	0.096	0.131	36.6
0.697	0.136	0.195	42.9

Table 3.1 suggests that the maximum power output of the turbine can be increased significantly by using a diffuser around the rotor. The increase of power output for each configuration can also be studied separately as a function of water velocity increase. The rate of power increase for each configuration as a function of the rate of water velocity increase is shown in Figure 3.14. To calculate each point of the plot in Figure 3.14, the comparison was performed between the each row of Table 3.1. According to Figure 3.14, the percentage of power increase due to the higher inflow velocity is larger when the diffuser was used in the system.

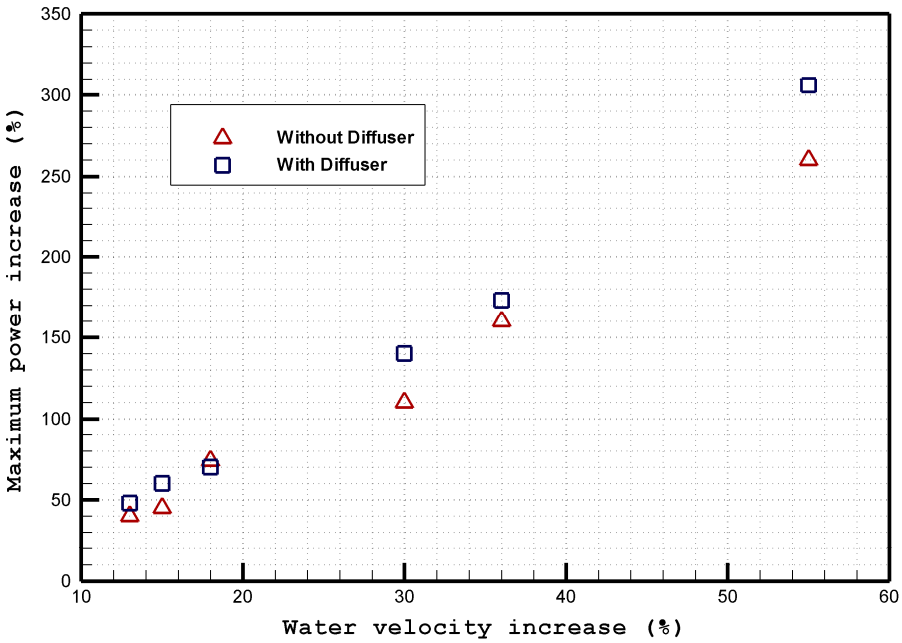

Figure 3.14 – The percentage of the power output increase versus the percentage of water velocity increase

Figure 3.15 presents the scatter plot of power coefficient as the function of tip-speed ratio for the turbine *with* and *without* a diffuser. According to Figure 3.15, the maximum Cp for the rotor without diffuser is about 0.26 for about λ=0.7 and for the rotor with diffuser is about 0.35 for λ=1.3. Thus the maximum power coefficient increased by 35% when the diffuser was mounted around the rotor.

The Cp plots in Figure 3.15 show that for $\lambda < 0.4$, the efficiency of both configurations (turbine with and without diffuser) is almost identical. However, the efficiency of the turbine without diffuser increased faster as λ increased.

For λ between 0.4 and 0.9, the efficiency (Cp) of the rotor without diffuser was higher than that of the rotor with diffuser. This phenomenon is related to formation of blockage vortices in the wake of the turbine with diffuser for low tip-speed ratios.

At λ = 1.05, the turbine with diffuser reached the maximum value of Cp for the rotor without diffuser. At λ > 1.4, the power coefficient decreased abruptly. Therefore, to obtain higher efficiency by using the diffuser, the working range of the turbine should correspond to the tip-speed ratios between 1.05 and 1.4.

The range of the tip-speed ratios for which the turbine performance is higher than 75% of the maximum value, is between λ = 0.45 to 0.9 for the rotor without diffuser and between λ = 1.05 to 1.4 for the rotor with diffuser.

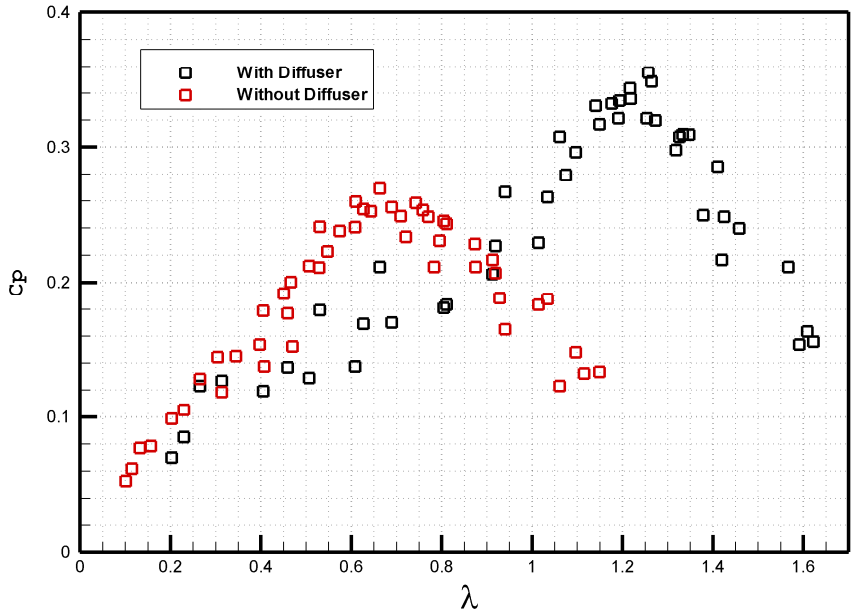

Figure 3.15 – Comparison of power coefficient of the turbine *with* and *without* diffuser as a function of the tip-speed ratio

3.6 Comparison of system size of the vertical axis wind turbine without and with diffuser

The system size of the turbine without and with diffuser can be calculated by using the performance curve presented in Figure 3.15. Since the data presented in Figure 3.15 is dimensionless, the data can be used for the full-scale turbine with the air as the working fluid. By considering the maximum power coefficient point as the working condition, the dimensions of the system can be calculated for different power outputs. Figure 3.16 shows the defined parameters for each configuration which are used in the following tables. Figure 3.16(a) illustrates D_1 as the diameter of the rotor without diffuser. Figure 3.16(b) illustrates three parameters, W_u, D_2 and W_d. W_u indicates the width of entrance of the diffuser at upstream, D_2 indicates the rotor diameter for the turbine with diffuser and W_d indicates the width of the turbine at downstream.

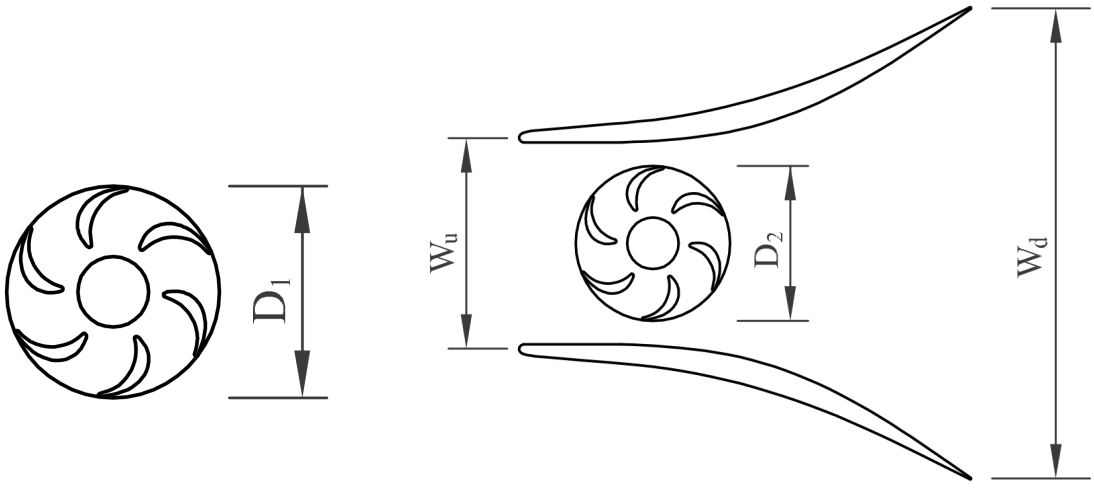

Figure 3.16 – System size parameters for a) turbine without diffuser b) turbine with diffuser

As it was discussed in the previous section, the maximum power coefficient of the turbine without diffuser is equal to 0.26 for λ=0.7. Furthermore, the maximum power coefficient for the turbine with diffuser is 0.35 for λ=1.3. The power coefficient values can be used in equation 3.2 to calculate the other parameters in the equation. For this calculation, the inflow air velocity of 10 m/s was considered. The power coefficient and the air density is also known for each configuration, therefore the swept area can be calculated as the function of power output. The swept area for the rotor without diffuser is equal to the rotor diameter multiplied by the rotor height, and for the turbine with diffuser - the entrance width of the diffuse (W_u) multiplied by the height of the rotor. The calculated swept areas for various power outputs are presented in Table 3.2. It can be observed that the swept area reduced by 25% when the diffuser was added around the rotor.

Table 3-2 - Swept area of the turbine with and without a diffuser for various power outputs

	Without diffuser	**With diffuser**
Power (W)	**Swept area A (m^2)**	**Swept area A (m^2)**
100	0.64	0.48
300	1.92	1.44
500	3.2	2.4
1000	6.4	4.8
5000	32	24
15000	96	72
25000	160	120

The swept area values in Table 3.2 can be used to calculate the dimensions of the turbine with the parameters introduced in Figure 3.16. These parameters are presented in Table 3.3. L1 and L2 in table 3.3 indicate the height of the turbine. According to these results, a 26% reduction in the rotor diameter and the rotor height can be achieved by implementing the diffuser.

Table 3-3 – System size of the turbine with and without a diffuser for various power outputs

	Without diffuser		**With diffuser**			
Power (W)	**D1 (m)**	**L1 (m)**	**D2 (m)**	**L2 (m)**	**Wu (m)**	**Wd (m)**
100	0.63	1.01	0.47	0.75	0.64	1.43
300	1.10	1.75	0.81	1.30	1.11	2.47
500	1.41	2.26	1.05	1.68	1.43	3.19
1000	2.00	3.20	1.48	2.37	2.02	4.51
5000	4.47	7.16	3.32	5.31	4.52	10.09
15000	7.75	12.39	5.74	9.19	7.84	17.48
25000	10.00	16.00	7.41	11.86	10.12	22.57

Chapter 4

Conclusions and recommendations

4.1 Summary

The performance of a novel vertical axis wind turbine (VAWT) was investigated experimentally using direct force measurements and particle image velocimetry (PIV). Two different configurations were considered. The first configuration involved a bare rotor, and the second one consisted of the same rotor enclosed in a diffuser. The objectives of the thesis are involved confirmation of the potential for power output increase by implementing the diffuser under the equivalent inflow conditions. Moreover, global, qualitative flow patterns downstream of the rotor were obtained and critically examined for each of the two configurations.

In the first part of the work, the power output and the power coefficient corresponding to each configuration (*without* and *with* the diffuser) were measured. The results were obtained by an experimental test inside a water tunnel with a small-scale turbine. The range of tip-speed ratios for the rotor without diffuser was from 0.1 to 1.15 and for the rotor with diffuser was from 0.2 to 1.62. As a result of these experiments, full performance curves were obtained for each of the two configurations.

According to the results obtained from the experiment, the maximum output power and the maximum power coefficient for the turbine without diffuser were observed at the tip-speed ratio of approximately 0.7. On the other hand, the maximum power and the maximum power coefficient of the turbine with diffuser were observed at the tip-speed ratio of approximately 1.25.

The comparison between the results for the rotor *without* and *with* the diffuser demonstrated 27% to 43% power output increase (depending on the inflow velocity) for the latter configuration. The maximum value of power coefficient for the turbine *without* diffuser was found to be equal to $C_p = 0.26$ for $\lambda = 0.7$, and the maximum value of power coefficient for the turbine *with* diffuser was found to be equal to $C_p = 0.35$ for $\lambda = 1.25$. Therefore, the maximum power coefficient was increased by 35% as a result of implementing the diffuser.

Furthermore, for $\lambda < 0.4$, the efficiency of the two configurations (*without* and *with* diffuser) was approximately the same. For the range of tip-speed ratios $0.4 < \lambda < 0.9$, the efficiency of the turbine *without* diffuser was larger than that of the diffuser-augmented turbine. In contrast, for the range of $1.05 < \lambda < 1.4$, the efficiency of the turbine *with* diffuser was higher than that of the turbine with bare rotor.

In the second part of the thesis, the flow patterns downstream of the rotor were studied in detail by using the PIV technique. Six different tip-speed ratios were considered for each configuration. The tip-speed ratios corresponded to the range of the parameters considered in the first part of the study, which dealt with the power output and the power coefficient trends.

The wake of the rotor *without* diffuser consisted of two shear layers. One of the shear layers (referred to as the upper shear layer in Chapter 3 section 3.4.2 and indicated in Figure 3.8) changed its orientation angle with respect to the inflow direction from +5° to -20° when the tip-speed ratio increased from $\lambda = 0.3$ to $\lambda = 1.15$. However, the other shear layer (referred to as the lower shear layer) had an orientation angle of -5° with respect to the inflow direction for the entire considered range of the tip-speed ratios.

In contrast, four shear layers were observed in the wake of the rotor *with* the diffuser. Two of the shear layers originated at the rotor, and the other two were formed at the diffuser. The shear layers that originated from the rotor eventually merged with the diffuser shear layers, and the orientation angle of the shear layers remained constant for the entire considered range of the tip-speed ratios. Therefore, in contrast to the case of the bare rotor, the turbine *with* the diffuser, produced a symmetric wake.

Finally, at low tip-speed ratios, blockage vortices were observed in the wake of both configurations. These vortices interfered with the flow passing through the rotor. The blockage vortices dissipated as the tip-speed ratios increased.

4.2 Recommendations for future work

The results of the current study indicated that the efficiency and the power output of a cross-flow turbine can be increased by adding a diffuser around the rotor. The diffuser profile was chosen arbitrary; therefore the shape of the diffuser was not optimized. As it was discussed in Chapter 1, there are several different diffuser designs which are

currently used in wind turbine applications. Also, different airfoil profiles should be tested as the diffuser for the presented turbine.

The diffuser optimization can be achieved by a computational fluid dynamics (CFD) study. Although CFD results should be validated by experimental tests, the presented PIV results can be used for that purpose. The validated CFD method can be subsequently used for further development of the diffuser.

Bibliography

1. Hills, R.L., *Power from Wind: A History of Windmill Technology*. 1996: Cambridge University Press.
2. *http://www.apakabardunia.com/post/arkeologi/7-karya-arsitektur-kuno-yang-menakjubkan#.*
3. Righter, R.W., *Wind Energy in America: A History*. 2003: University of Oklahoma Press.
4. Spera, D.A., *Wind Turbine Technology: Fundamental Concepts of Wind Turbine Engineering.* American Society of Mechanical Engineers, 1994.
5. Burton, T., Sharpe, D., Jenkins, N. and Bossanyi, E., *Wind Energy Handbook* 2001: John Wiley & Sons, Ltd.
6. Paraschivoiu, I., *Wind Turbine Design with emphasis on darrieus concept*. 2002: Polytechnic international press.
7. Kirke, B., *Developments in ducted water current turbines.* U. of South Australia, 2005.
8. Riegler, G., *Principles of energy extraction from a free stream by means of wind turbines.* Wind Engineering, 1983. **7**: p. 115-126.
9. Igra, O., *The shrouded aerogenerator*. Energy, 1977. **2**(4): p. 429-439.
10. Igra, O., *Research and development for shrouded wind turbines.* Energy Cont. & Momt, 1981. **21**: p. 13-48.
11. Abe, K., Nishidab, M., Sakuraia, A., Ohyac, Y., Kiharaa, H., Wadad, E. and Satod, K., *Experimental and numerical investigations of flow fields behind a small wind turbine with a flanged diffuser*. Journal of Wind Engineering and Industrial Aerodynamics, 2005. **93**(951–970).
12. Ohya, Y., Karasudani, T., Sakurai, A., Abe, K. and Inoue, M., *Development of a shrouded wind turbine with a flanged diffuser.* Journal of Wind Engineering and Industrial Aerodynamics, 2008. **96**: p. 524-539.
13. Ohya, Y. and Karasudani, T., *A shrouded wind turbine generating high output power with wind-lens technology.* Renewable Energy, 2010.

14. Takahashi, S., Ohya, Y., Karasudani, T. and Watanabe, K., *Numerical and experimental studies of airfoils suitable for Vertical Axis Wind Turbines and an application of wind-energy collecting structure for higher performance.* International Association of Wind engineering, 2006.
15. Roa, A.M., Aumelas, V., Maitre, T. and Pellone, C., *Numerical and experimental analysis of a darrieus-type cross flow water turbine in bare and shrouded configurations.* IOP Conf. Series: Earth and Environmental Science, 2010. **12**.
16. Whale, J., Andersonb, C. G., Bareissc, R. and Wagnerc, S., *An experimental and numerical study of the vortex structure in the wake of a wind turbine.* Journal of Wind Engineering and Industrial Aerodynamics, 2000. **84**.
17. Whale, J., Papadopoulosb, K. H., Andersonc, C. G., Helmisb, C. G. and Skynera, D. J., *A study of the wake structure of a wind turbine comparing measurements from laboratory and full-scale experiments.* Sol. Energy Eng., 1996. **56**(6): p. 621-633.
18. Grant, I. and Parkin, P., *A DPIV study of the trailing vortex elements from the blades of a horizontal axis wind turbine in yaw.* Experiments in Fluids, 2000. **28**: p. 368-376.
19. Toshimitsu, K., Nishikawa, K., Haruki, W., Oono, S., Takao, M., and Ohya, Y., *PIV measurements of flows around the wind turbines with a flanged-diffuser shroud.* Journal of Thermal Science, 2008. **17**: p. 375-380.
20. Fujisawa, N., *Velocity measurements and numerical calculations of flow fields in and around Savonius rotors* Journal of Wind Engineering and Industrial Aerodynamics, 1996. **59**: p. 39-50.
21. Saha, U.K., *On the performance analysis of Savonius rotor with twisted blades.* Renewable Energy, 2006. **31**: p. 1776–1788.
22. Murai, Y., Nakada, T., Suzuki, T., and Yamamoto, F., *Particle tracking velocimetry applied to estimate the pressure field around a Savonius turbine.* Measurement science and technology, 2007. **18**: p. 2491–2503.

23. Ferreira, C.S., van Kuik, G., van Bussel, G., and Scarano, F., *Visualization by PIV of dynamic stall on a vertical axis wind turbine.* Experiments in Fluids, 2008. **46**: p. 97-108.

24. Ferreira, C.S., van Zuijlen, A., Bijl, H., van Bussel, G. and van Kuik, G., *Simulating dynamic stall in a two-dimensional vertical-axis wind turbine: verification and validation with particle image velocimetry data.* Wind Energ., 2010. **13**: p. 1-17.

25. Shibuya, S. Fujisawa, N. and Takano, T., *Visualization and PIV measurement of unsteady flow around a Daerrieus wind turbine in dynamic stall*. 7th international conference on Nuclear Engineering. 1999.

26. Fujisawa, N., *Observations of dynamic stall on Darrieus wind turbine blades.* Journal of Wind Engineering and Industrial Aerodynamics, 2001. **89**: p. 201-214.

27. Raffel, M., Willert, C. and J. Kompenhans, J., *Particle Image Velocimetry: A Practical Guide*. 2002: Springer.

28. Adrian, R.J., *Particle-imaging techniques for experimental fluid mechanics.* Annu. Rev. Fluid Mech, 1991. **23**: p. 261-304.

29. Adrian, R.J., *Twenty years of particle image velocimetry.* Experiments in Fluids, 2005. **39**: p. 159-169.

30. Huang, H.T., Fiedler, H.E. and Wang, J.J., *Limitation and improvement of PIV.* Experiments in Fluids, 1993. **15**: p. 168-174.

31. Utami, T., Blackwelder, R.F., and Ueno, T., *A cross-correlation technique for velocity field extraction from particulate visualization.* Experiments in Fluids, 1991. **10**: p. 213-223.

32. Burch, J.M., *Production of multiple beam fringes from photographic scatters.* Journal of Modern Optics, 1968. **15**(2): p. 101-111.

33. Willert, C.E., and Gharib, M., *Digital particle image velocimetry.* Experiments in Fluids, 1991. **10**: p. 181-193.

34. White, F., *Fluid Mechanics 6th edition*. 2006: McGraw-Hill Science / Engineering / Math.

35. Bouhadji, L. and Oshkai, P., *Numerical and Experimental Investigation of a Wind Power Generator Design*, in *Department of Mechanical Engineering*. 2007, University of Victoria: Victoria, BC.

36. Okajima, A., Donglai, Y.i., Sakuda, A., and Nakano, T., *Numerical study of blockage effects on aerodynamic characteristics of an oscillating rectangular cylinder.* Journal of Wind Engineering and Industrial Aerodynamics, 1997. **67&68**: p. 91-102.

37. Norberg, C., *Flow around rectangular cylinders: Pressure forces and wake frequencies.* Journal of Wind Engineering and Industrial Aerodynamics, 1993. **49**: p. 187-196.

38. Ewald, B.F.R., *Wind Tunnel Wall Correction.* AGARDograph 336, 1998.

39. Mikkelsen, R., *Actuator Disc Methods Applied to Wind Turbines*, in *Mechanical Engineering* 2003, Technical University of Denmark.

40. Sorensen, J.N., Shen, W.Z., and Mikkelsen, R., *Wall Correction Model for Wind Tunnels with Open Test Section.* AIAA JOURNAL, 2006. **44**(8).

41. Wilson, R.E. and Lissaman, P.B.S., *Applied aerodynamics of wind power machines*. 1974. p. 106.

42. Islam, M., Tinga, D.S.K and Fartaja, A. *Aerodynamic models for Darrieus-type straight-bladed vertical axis wind turbines.* Renewable and Sustainable Energy Reviews, 2008. **12**: p. 1087-1109.

43. Templin, R.J., *Aerodynamic performance theory for the NRC vertical-axis wind turbine*, in *NRC Lab. LTR-LA-190*. 1970.

44. Wilson, R.E. and Lissaman, P.B.S. *Applied aerodynamics of wind power machines.* Oregon State University, 1974.

45. Paraschivoiu, I., *Double-multiple streamtube model for darrieus wind turbines*, in *Second DOE/NASA wind turbines dynamics workshop*. 1981: Cleveland, OH.

46. Paraschivoiu, I. and Delclaux, F., *Double multiple streamtube model with recent improvements.* J Energy, 1983. **7**: p. 250-255.

47. Strickland, J.H., Webster, B.T. and Nguyen, T., *A Vortex model of the darrieus turbine: an analytical and experimental study*. J Wind Eng, 1979. **101**: p. 500-505.